Ocean Engineering 288 (2023) 116016

Contents lists available at ScienceDirect

Ocean Engineering

journal homepage: www.elsevier.com/locate/oceaneng

Reduced order modeling of hydrodynamic interactions between a submarine and unmanned underwater vehicle using non-myopic multi-fidelity active learning

Brady Hammond [a,b,*], Themistoklis P. Sapsis [b]

[a] United States Navy, USA
[b] Department of Mechanical Engineering, Massachusetts Institute of Technology, Cambridge, MA 02138, USA

ARTICLE INFO

Keywords:
Reduced order modeling of hydrodynamic interactions
Unmanned underwater vehicles
Non-myopic active learning
Multi-fidelity Gaussian process regression

ABSTRACT

Several efforts have been dedicated to developing computational tools capable of predicting the hydrodynamic forces and moments of Unmanned Underwater Vehicles (UUVs). However, there is no method at the moment that allows for real-time computational modeling of all the complex hydrodynamic interaction forces and moments that a UUV experiences when operating in close proximity to a moving submarine. Real-time modeling of these hydrodynamic interactions is essential to simulate the motion required to launch and recover UUVs from submarines. Potential flow models are often fast enough to be used in real time, but lack the accuracy of Computational Fluid Dynamics (CFD) simulations, which often take hours or days to solve. Here, we formulate the problem in the context of machine learning, specifically active learning. The goal is to develop a surrogate model capable of predicting the UUV and submarine hydrodynamic interactions in real time using a very small number of carefully selected CFD simulations. We introduce a new active learning framework called Non-Myopic Multi-Fidelity Active Learning for Gaussian Process (GP) regression that accelerates the convergence of the surrogate model by utilizing the low cost of the low fidelity simulations to explore the domain, as well as optimally selected high fidelity simulations to improve the model accuracy. The resulting surrogate model can be integrated into UUV control and autonomy systems and motion simulators to further enable UUV launch and recovery from submarines. This new active learning method may also be used to create higher accuracy and lower cost surrogate models in other real world applications.

1. Introduction

In order to enable the launch and recovery of UUVs from submarines, a UUV needs to be able to overcome the hydrodynamic interaction forces and moments between the two vehicles (Leong, 2014). These hydrodynamic interactions are often predicted using high fidelity CFD modeling due to its high accuracy. While most CFD simulations take hours to days to complete, a UUV control system needs to respond within milliseconds in order to maintain the desired trajectory. As such, the UUV needs to determine the hydrodynamic interaction forces and moments in real time based on its position, heading, speed, and proximity to its desired path.

Modeling loads on the UUV can be performed with a variety of computational models that resolve the governing fluid equations. These range from low fidelity and low cost models to more expensive and more accurate models. Specifically, low fidelity models, such as potential flow solvers use simplified physics which neglects viscosity, skin friction, boundary layer development, flow separation, and leads to the d'Alembert paradox which predicts zero drag on a UUV moving at constant velocity (Newman, 2017; Fossen, 2011). These low fidelity solvers are often improved and supplemented with simple parametric models to help overcome these weaknesses and often have the capability to be solved in real time (Anon, 2018). However, they ultimately lack the accuracy needed to model the complex real world hydrodynamic interactions to enable UUV launch and recovery operations. This can be achieved by CFD solvers that rigorously model all the important fluid mechanics phenomena, but they have significant computational cost. Because the required accuracy of the CFD is not capable of being delivered in real time, a surrogate model is needed that is capable of being implemented in real time and has the accuracy of the CFD. While CFD may be performed by some potential flow solvers, the term CFD for this study refers to the high fidelity computational methods that use the Reynolds-averaged Navier–Stokes equations to resolve the UUV hydrodynamics. The potential flow solver refers to the low fidelity

---

[*] Corresponding author at: Department of Mechanical Engineering, Massachusetts Institute of Technology, Cambridge, MA 02138, USA.
E-mail address: bhammond@mit.edu (B. Hammond).

https://doi.org/10.1016/j.oceaneng.2023.116016
Received 16 December 2022; Received in revised form 1 September 2023; Accepted 8 October 2023

model that assumes the fluid is inviscid and determines UUV drag using built-in empirical models.

A typical approach for building a surrogate model is to collect high fidelity data, i.e. from expensive and highly accurate CFD solvers, and apply reduced order modeling ideas. As such, this study uses the terms surrogate model and reduced order model interchangeably. However, even in an offline setting (i.e. just to produce training data), the computational cost of CFD can be prohibitive, given that the parameter space for a UUV is pretty significant (Leong, 2014; Fedor, 2009). For such a case, an alternative is to combine a few, carefully selected simulations from a CFD model with plenty of low fidelity computations, e.g. from a potential flow solver. Integrating various fidelity models into one surrogate is known as multi-fidelity modeling (Perdikaris et al., 2015; Kennedy, 2000). By leveraging data from a lower cost and less accurate model with data from a high fidelity model, the accuracy of the surrogate model can be improved without the need for an excessive number of high fidelity simulations. This results in a significant reduction of the computational cost of the surrogate model without sacrificing accuracy.

An important question for developing accurate surrogate models is the selection of the most informative training data, i.e. what CFD simulations one should perform to get the most important information. This can be achieved by employing active learning, a type of machine learning data sampling method in which the algorithm is able to determine the optimal set of input parameters for which the next simulation should be performed (Sacks et al., 1989; Chaloner and Verdinelli, 1995; Blanchard and Sapsis, 2021). Typical active learning algorithms are characterized by myopia, or nearsightedness: a condition in which lack of foresight can inhibit the ability of a sampling algorithm to select the optimal sampling location for the surrogate model (Gonzalez et al., 2015; Jiang et al., 2017). For example, a game exists where an unknown random number is selected between 0 and 100. The object of the game is to minimize the value between a number chosen by the participant and the unknown random number. In this instance, the optimal number to select would be 50, halfway between the two endpoints. This ensures that the maximum error between any random number and the selected value is 50. Now assume the participant is allowed to select a second number. Once 50 is selected, the next optimal value would be either 25 or 75. However, neither of these two options reduces the maximum error because there is still the potential to be off by 50. This problem exists because of myopia. Originally, the participant is only considering selecting one single number. If the selection method is non-myopic, there are different optimal values chosen. By knowing beforehand that two selections would be made, the optimal selections would be at 25 and 75. By selecting these two points, the maximum value between any random number and one of the selected values would be 25. This illustrates how having the foresight of knowing about future sampling characteristics provides a different set of optimal sampling locations.

This paper introduces the use of a non-myopic multi-fidelity active learning GP regression algorithm for reduced order modeling and compares it with standard myopic active learning techniques. We begin with a quick review of Gaussian process regression, multi-fidelity modeling, and active learning in a myopic and non-myopic setup. In Section 3, we present the formulation and implementation of the method, and subsequently, in Sections 4 and 5, we examine its relative advantages in the context of standard benchmark functions and prototype problems for scalar and vector outputs. In Section 6, we examine its performance and demonstrate its favorable properties in the context of reduced order modeling for UUV and submarine hydrodynamic interactions.

2. Background

2.1. Gaussian process regression

The purpose of GP regression is to develop a reduced order model that is capable of predicting the value of dependent variables based on the input of independent variables. GP regression is a non-parametric technique. This means that it does not require the developer to design a model structure because the structure is determined by the data. In contrast to typical regression methods, GP provides rigorous estimates for the epistemic uncertainty of the derived model, i.e. errors due to lack of data. The GP regression model can be expressed as a random function,

$$y = f(x) + \epsilon \tag{1}$$

where $x \in \mathbb{R}^d$, $\epsilon \sim \mathcal{N}(0, \sigma^2)$ represents the noise of the model and the random function f follows a Gaussian distribution with prescribed mean and covariance function (Rasmussen and Williams, 2006):

$$f(x) \sim \mathcal{GP}(\mu(x), k(x, x')), \tag{2}$$

where $\mu(x)$ is the mean and $k(x, x')$ the covariance:

$$\mu(x) = \mathbb{E}[f(x)] \tag{3}$$

$$k(x, x') = \mathbb{E}[(f(x) - \mu(x))(f(x') - \mu(x'))] \tag{4}$$

There are many different covariance functions (or kernels) that are often used in GP models. Some of the more popular kernels include the white noise kernel, squared exponential kernel, rational quadratic kernel, and the periodic kernel (Wilson and Adams, 2013). Rather than explore the impact of these different kernels, this study uses the popular radial basis function (RBF) kernel with automatic relevance determination:

$$k(x, x') = \exp\left(\frac{-(x - x')^T \lambda^{-1} (x - x')}{2}\right) \tag{5}$$

where λ is the diagonal matrix containing the length scales of each input dimension. This kernel is selected because it simulates a Bayesian linear regression model with an infinite number of basis functions. In other words, this kernel can be formed from a linear combination of an infinite number of Gaussian-shaped basis functions (Rasmussen and Williams, 2006). Because an infinite number of these basis functions can determine the form of any (sufficiently smooth) output function, this method is well suited for this study with an unknown form of the different output functions. Automatic relevance determination is used because it enables the GP regression kernel to have different length scales for each input dimension.

GP regression is ultimately used to calculate the predicted mean $y(\mathbf{X}_*)$ and covariance $K_{yy}(\mathbf{X}_*, \mathbf{X}'_*)$ when conditioning on a set of input–output data pairs. In particular, the model is trained with a data set $\mathcal{D} = \{x_i, y_i\}_{i=1}^n$, where n is the number of samples. We also use the notation $\mathbf{X} = [x_1, \ldots, x_n] \in \mathbb{R}^{d\times n}$ and $\mathbf{y} = [y_1, \ldots, y_n] \in \mathbb{R}^n$ where bold represents a matrix or vector. Likewise, $\mathbf{X}_* = [x_{*1}, \ldots, x_{*m}] \in \mathbb{R}^{d\times m}$, is a set of m locations within the $d-$dimension domain for which a prediction is desired. Eqs. (6) and (7) determine the predicted mean and covariance at a set of points $\mathbf{X}_*$ (Rasmussen and Williams, 2006):

$$y(\mathbf{X}_*) = K(\mathbf{X}_*, \mathbf{X})[K(\mathbf{X}, \mathbf{X}) + \sigma_n^2 \mathbf{I}]^{-1} \mathbf{y} \tag{6}$$

$$K_{yy}(\mathbf{X}_*, \mathbf{X}'_*) = K(\mathbf{X}_*, \mathbf{X}'_*) - K(\mathbf{X}_*, \mathbf{X})[K(\mathbf{X}, \mathbf{X}) + \sigma_n^2 \mathbf{I}]^{-1} K(\mathbf{X}, \mathbf{X}'_*) \tag{7}$$

The term σ_n^2 represents the aleatoric uncertainty or inherently random effects of the outcome of an experiment. It is a hyperparameter that is optimized using gradient descent methods to improve the predictive capabilities of the GP regression (Rasmussen and Williams, 2006). Additionally, it helps ensure the matrix in brackets in Eqs. (6) and (7) is well conditioned.

2.2. Active learning

For many problems, like the one considered here, the cost of obtaining accurate training data for a GP regression is very large. As such, each new data point is selected sequentially and methodically, so that

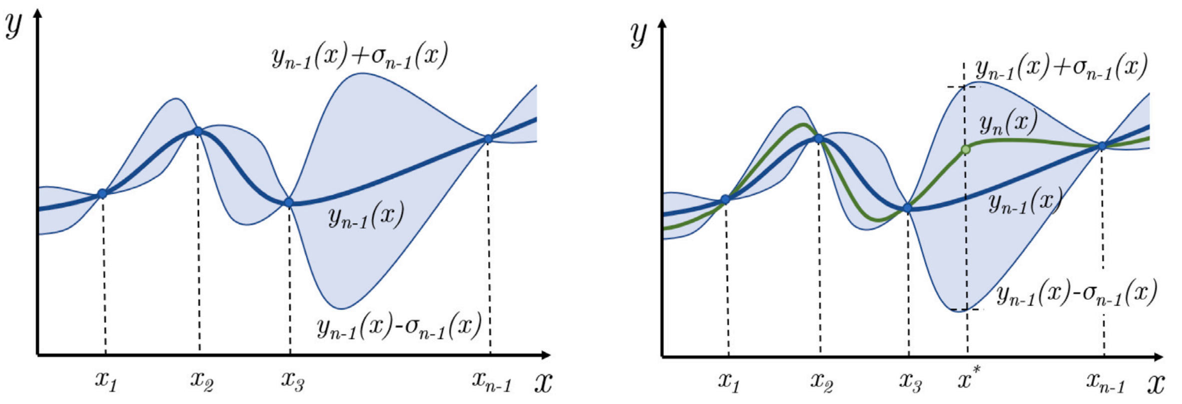

(a) Estimation of the surrogate predicted mean y_{n-1} and its error σ_{n-1}

(b) Sampling at a new optimal location x^* and estimation of new surrogate predicted mean y_n

Fig. 1. Demonstration of active sampling method of determining the optimal sample location and updating the predicted mean of the surrogate model.

it provides the most improvement to the surrogate model. This type of data sampling method in which the algorithm is able to determine the optimal set of input parameters for the next sample is called active learning or optimal experimental design (Sacks et al., 1989; Chaloner and Verdinelli, 1995).

Suppose we have a GP regression model $y_{n-1}(x)$ with an error of $\sigma_{n-1}(x) = \sqrt{K_{yy}(x,x)}$ trained from a data set with input vectors $\{x_1, x_2, \dots, x_{n-1}\}$. The aim in active learning is to use the predicted mean and error estimate, to optimize the selection of the next sample, x^*. Specifically, active learning uses what is called an acquisition function $q(x|y_{n-1}, \sigma_{n-1})$ in order to determine this next optimal sample x^* as below:

$$x^* = \arg\max q(x|y_{n-1}, \sigma_{n-1}). \tag{8}$$

Once this optimal sampling location x^* is determined, the sample is taken at that point and the new data is added to the existing data set $\mathcal{D}_n = \{\mathcal{D}_{n-1} \cup (x^*, y^*)\}$. The new surrogate mean $y_n(x)$ and error $\sigma_n(x)$ are determined and the process is iterated as necessary. Fig. 1 illustrates the active sampling process.

In Fig. 1, the optimal sampling location x^* is determined by locating the point in the domain with the largest model error σ_{n-1}. This popular acquisition function is known as Uncertainty Sampling (US) and is shown in Eq. (9), Blanchard and Sapsis (2021).

$$q_{US}(x) = \sigma^2(x) \tag{9}$$

The uncertainty sampling acquisition function is widely used because it is intuitive, robust, broadly applicable, inexpensive to compute, and has analytical gradients, which allows the use of gradient-based optimizers so it becomes considerably more efficient than other acquisition functions (Gramacy and Lee, 2009). There are many different acquisition functions like integrated variance reduction, input-weighted integrated variance reduction, mutual information, and likelihood-weighted acquisition functions (Blanchard and Sapsis, 2021). However, for the purpose of this study in which non-myopic active learning is explored, only the uncertainty sampling acquisition function is used due to its robustness.

2.3. Myopic versus non-myopic active learning algorithms

Typical active learning sampling methods are myopic or "near-sighted". This means they only consider a single step into the future when selecting the next optimal sampling location (Gonzalez et al., 2015). Once a location is selected, the output is evaluated at that single point and this new data is added to the existing data set. In particular, when a new single location x_n is determined using active learning criteria, the output y_n is computed from a simulation or experiment, and the data set is augmented with the new information, i.e. $\mathcal{D}_n = \{\mathcal{D}_{n-1} \cup (x_n, y_n)\}$. Fig. 2 illustrates this myopic sampling algorithm.

While this myopic approach is often used in practice, there are other non-myopic approaches that provide solutions to the multi-step look-ahead problem with better results than a myopic approach (Gonzalez et al., 2015; Jiang et al., 2017). Specifically, a non-myopic approach enables the algorithm to determine the next optimal sampling location based on the influence of several future potential sampling locations. This allows the algorithm to select the optimal sampling location with the knowledge about how the many future sampling locations may influence the next sample. This influence of future evaluations on current sampling locations is illustrated in Fig. 3 using a blue line.

There are many different non-myopic algorithms that use various acquisition functions to evaluate the impact of future samples (Gonzalez et al., 2015; Jiang et al., 2017; Osborne et al., 2008; Morere et al., 2016). These acquisition functions vary in how they evaluate and utilize the expected value of the future samples on the model. For example, one approach is to develop a look-ahead loss function that considers the cost or penalty of future samples. However, all of these non-myopic sampling methods are only used for single fidelity surrogate models and do not offer a means to which non-myopic methods can be expanded to operate between models of different fidelity. In this study, we explore a new sampling method by bridging the gap between non-myopic sampling and multi-fidelity GP modeling to achieve improvements in lowering the cost and increasing the accuracy of high fidelity simulators.

2.4. Multi-fidelity modeling

Multi-fidelity GP modeling uses multiple separate simulators or experiments to develop the surrogate model. Like in the present context, there is a high fidelity model which is computationally expensive to use and a low fidelity model which requires much less computational effort to perform. In the context of this work, the high fidelity simulation is CFD and the low fidelity simulation is a potential flow solver. Because of the different assumptions and physics being modeled, the CFD and potential flow simulators produce different results for any given sampling location. These results are stored in a high fidelity data set denoted by $\mathcal{D}_{\mathcal{HF}} = \{\mathbf{X}_{\mathcal{HF}}, \mathbf{y}_{\mathcal{HF}}\}$ and a low fidelity data set $\mathcal{D}_{\mathcal{LF}} = \{\mathbf{X}_{\mathcal{LF}}, \mathbf{y}_{\mathcal{LF}}\}$. Kennedy and O'Hagan developed the following first-order auto-regressive co-kriging scheme for the relationship between high and low fidelity models (Kennedy, 2000).

$$f_{\mathcal{HF}}(\mathbf{X}_*) = \rho(\mathbf{X}_*) f_{\mathcal{LF}}(\mathbf{X}_*) + \delta(\mathbf{X}_*) \tag{10}$$

The functions $f_{\mathcal{HF}}(\mathbf{X}_*)$ and $f_{\mathcal{HF}}(\mathbf{X}_*)$ represent the GP regression models trained on the high fidelity and low fidelity data sets respectively. The $\delta(\mathbf{X}_*)$ is a GP regression model that is independent of

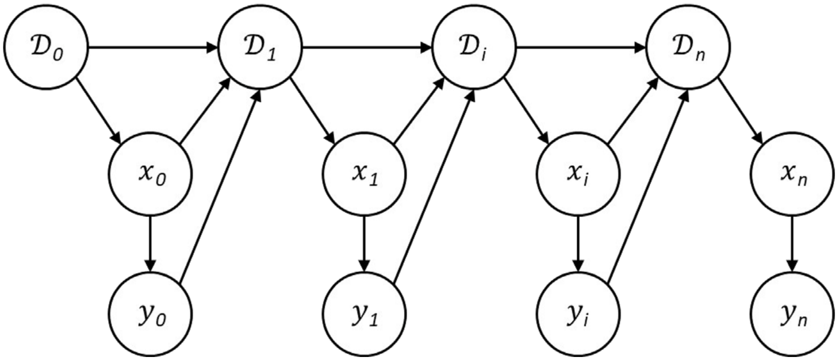

Fig. 2. Myopic sampling algorithm: At every step, an active learning criterion determines a single new input x_n, for which we obtain the output y_n. Recall that $\mathcal{D}_i$ is the data set of the inputs and outputs.

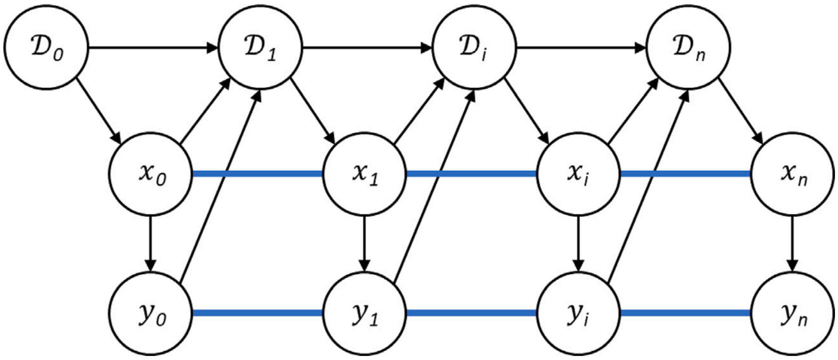

Fig. 3. Non-myopic sampling algorithm: The next sample is influenced by potential locations of future samples. This allows the method to consider the impact of future results beyond the capability of myopic sampling.

both $f_{\mathcal{HF}}(\mathbf{X}_*)$ and $f_{\mathcal{HF}}(\mathbf{X}_*)$. The ρ parameter is a scaling factor that correlates the high fidelity and low fidelity models. This scaling factor is set to unity for the purposes of this study because the high fidelity CFD model and the low fidelity potential flow model both compute the same forces so no scaling is needed between the different fidelity simulators (Kennedy, 2000). Using a multi-fidelity modeling approach provides the benefit of improving the accuracy and cost by combining expensive accurate high-fidelity data with cheaper and less accurate low-fidelity data (Kennedy, 2000; Grassi et al., 2020; Takeno et al., 2020). This scheme and the others can be used recursively to account for more than two levels of fidelity, but only two levels are used for this study. There are other schemes to account for multi-fidelity modeling besides the first-order auto-regressive co-kriging scheme. These other schemes include a deep GP in which the scaling factor is replaced with an unknown function $z(f_{\mathcal{LF}}(x))$ which maps the difference between the low and high fidelity models (Damianou and Lawrence, 2013). This function z is often another GP regression, which is why this is often called deep GP regression, but the added layer of GP regression comes at a steep computational price. Another scheme is the nonlinear auto-regressive multi-fidelity GP regression scheme in which a higher dimension GP regression model is created that jointly relates the input space and the outputs of the lower fidelity level to the output of the higher fidelity model. Once again, this modification to the multi-fidelity modeling scheme increases the computational cost of the model (Perdikaris et al., 2017).

As such, the first-order auto-regressive co-kriging scheme is used for this study due to its low cost and ease of implementation (Kennedy, 2000; Damianou and Lawrence, 2013; Perdikaris et al., 2017). Eq. (10) implies the Markov property: given $f_{\mathcal{LF}}(\mathbf{X}_*)$ we can learn nothing more about $f_{\mathcal{HF}}(\mathbf{X}_*)$ from any other model output $f_{\mathcal{LF}}(\mathbf{X}'_*)$ for $\mathbf{X}_* \neq \mathbf{X}'_*$, i.e $\mathrm{cov}\{f_{\mathcal{HF}}(\mathbf{X}_*), f_{\mathcal{LF}}(\mathbf{X}'_*)|f_{\mathcal{LF}}(\mathbf{X}_*)\} = 0$, Kennedy (2000).

This allows for the following definition of the high fidelity $f_{\mathcal{HF}}(\mathbf{X}_*)$, low fidelity $f_{\mathcal{LF}}(\mathbf{X}_*)$, multi-fidelity $f_{\mathcal{MF}}(\mathbf{X}_*)$, and $\delta(\mathbf{X}_*)$ GP regression models:

$$\begin{aligned}
f_{\mathcal{HF}}(\mathbf{X}_*) &\sim \mathcal{GP}(y_{\mathcal{HF}}(\mathbf{X}_*), K_{yy,\mathcal{HF}}(\mathbf{X}_*, \mathbf{X}'_*)) \\
f_{\mathcal{LF}}(\mathbf{X}_*) &\sim \mathcal{GP}(y_{\mathcal{LF}}(\mathbf{X}_*), K_{yy,\mathcal{LF}}(\mathbf{X}_*, \mathbf{X}'_*)) \\
\delta(\mathbf{X}_*) &\sim \mathcal{GP}(y_{\delta}(\mathbf{X}_*), K_{yy,\delta}(\mathbf{X}_*, \mathbf{X}'_*)) \\
f_{\mathcal{MF}}(\mathbf{X}_*) &\sim \mathcal{GP}(y_{\mathcal{MF}}(\mathbf{X}_*), K_{yy,\mathcal{MF}}(\mathbf{X}_*, \mathbf{X}'_*)) \\
\text{where} \quad & y_{\mathcal{MF}}(\mathbf{X}_*) = y_{\mathcal{LF}}(\mathbf{X}_*) + y_{\delta}(\mathbf{X}_*) \\
\text{and} \quad K_{yy,\mathcal{MF}}(\mathbf{X}_*, \mathbf{X}'_*) &= K_{yy,\mathcal{HF}}(\mathbf{X}_*, \mathbf{X}'_*) = K_{yy,\delta}(\mathbf{X}_*, \mathbf{X}'_*)
\end{aligned} \tag{11}$$

By expanding Eqs. (2), (6), (7), and (10) to account for the multi-fidelity modeling approach, the predicted mean and covariance of the low and high fidelity GP models are derived. Additionally, the $\delta(\mathbf{X}_*)$ GP regression model from Eq. (10) has a predicted mean and covariance listed in Eq. (14). In order to determine the mean of the $\delta(\mathbf{X}_*)$ GP regression model, a vector of the outputs $\mathbf{y}_\delta$ is needed. This is found by using the difference between the high fidelity and low fidelity outputs for each of the n high fidelity samples at the corresponding low fidelity sample locations as shown in Eq. (15). This requires that the samples of the high fidelity data set are a subset within the low fidelity data set, i.e $\mathbf{X}_{\mathcal{LF}} \subseteq \mathbf{X}_{\mathcal{HF}}$.

$$
\begin{aligned}
y_{\mathcal{HF}}(\mathbf{X}_*) &= K(\mathbf{X}_*, \mathbf{X}_{\mathcal{HF}})[K(\mathbf{X}_{\mathcal{HF}}, \mathbf{X}_{\mathcal{HF}}) \\
&\quad + \sigma_n^2 \mathbf{I}]^{-1} \mathbf{y}_{\mathcal{HF}} \\
K_{yy,\mathcal{HF}}(\mathbf{X}_*, \mathbf{X}_*') &= K(\mathbf{X}_*, \mathbf{X}_*') - K(\mathbf{X}_*, \mathbf{X}_{\mathcal{HF}})[K(\mathbf{X}_{\mathcal{HF}}, \mathbf{X}_{\mathcal{HF}}) + \sigma_n^2 \mathbf{I}]^{-1} \\
&\quad \times K(\mathbf{X}_{\mathcal{HF}}, \mathbf{X}_*') \\
\sigma_{\mathcal{HF}}(\mathbf{X}_*) &= \sqrt{K_{yy,\mathcal{HF}}(\mathbf{X}_*, \mathbf{X}_*)}
\end{aligned}
\tag{12}
$$

and

$$
\begin{aligned}
y_{\mathcal{LF}}(\mathbf{X}_*) &= K(\mathbf{X}_*, \mathbf{X}_{\mathcal{LF}})[K(\mathbf{X}_{\mathcal{LF}}, \mathbf{X}_{\mathcal{LF}}) \\
&\quad + \sigma_n^2 \mathbf{I}]^{-1} \mathbf{y}_{\mathcal{LF}} \\
K_{yy,\mathcal{LF}}(\mathbf{X}_*, \mathbf{X}_*') &= K(\mathbf{X}_*, \mathbf{X}_*') - K(\mathbf{X}_*, \mathbf{X}_{\mathcal{LF}})[K(\mathbf{X}_{\mathcal{LF}}, \mathbf{X}_{\mathcal{LF}}) + \sigma_n^2 \mathbf{I}]^{-1} \\
&\quad \times K(\mathbf{X}_{\mathcal{LF}}, \mathbf{X}_*') \\
\sigma_{\mathcal{LF}}(\mathbf{X}_*) &= \sqrt{K_{yy,\mathcal{LF}}(\mathbf{X}_*, \mathbf{X}_*)}
\end{aligned}
\tag{13}
$$

and

$$
\begin{aligned}
y_{\delta}(\mathbf{X}_*) &= K(\mathbf{X}_*, \mathbf{X}_{\mathcal{HF}})[K(\mathbf{X}_{\mathcal{HF}}, \mathbf{X}_{\mathcal{HF}}) + \sigma_n^2 \mathbf{I}]^{-1} \mathbf{y}_{\delta} \\
K_{yy,\delta}(\mathbf{X}_*, \mathbf{X}_*') &= K_{yy,\mathcal{HF}}(\mathbf{X}_*, \mathbf{X}_*) \\
\sigma_{\delta}(\mathbf{X}_*) &= \sqrt{K_{yy,\delta}(\mathbf{X}_*, \mathbf{X}_*)}
\end{aligned}
\tag{14}
$$

and

$$
\mathbf{y}_{\delta} = \{y_{\mathcal{HF},i} - y_{\mathcal{LF},i}\}_{i=1}^{n} \tag{15}
$$

Eq. (11) through (15) provide the predicted mean and covariance for all of the elements used in multi-fidelity GP regression. In summary, this multi-fidelity GP regression framework outlined simply in Eq. (10) can be used to construct probabilistic models that enable the combination of high and low fidelity simulators. This utilizes the benefits of the different fidelity simulators by capturing the high accuracy and low computational cost from the high and low fidelity simulators respectively. This framework provides the grounds for which the non-myopic active sampling concept can be incorporated into a multi-fidelity GP regression scheme to improve the cost and accuracy of the surrogate model.

3. Non-myopic multi-fidelity active learning

3.1. Inter-model acquisition function

Motivated by the advantage of producing a low cost and high accuracy surrogate model using the multi-fidelity framework, as well as a non-myopic setup for active learning, we proceed with the formulation of a non-myopic multi-fidelity active learning algorithm. Before the algorithm can be formalized, we must introduce a new type of acquisition function called an inter-model acquisition function q_{IM}. It is used to determine the next location for the high fidelity simulation to be performed. This new type of acquisition function takes into account the statistics of multiple GP regression models with differing fidelity, rather than a single fidelity GP regression model like other acquisition functions. The general form of the inter-model acquisition function is as follows:

$$
q_{IM}(\mathbf{X}_*) = f(y_{\mathcal{HF}}(\mathbf{X}_*), \sigma_{\mathcal{HF}}(\mathbf{X}_*) = \sigma_{\delta}(\mathbf{X}_*), y_{\mathcal{LF}}(\mathbf{X}_*), \sigma_{\mathcal{LF}}(\mathbf{X}_*), y_{\delta}(\mathbf{X}_*)). \tag{16}
$$

In order to formulate an effective inter-model acquisition function, consider an example high fidelity and a multi-fidelity GP regression model. Recall from Eqs. (11) and (14) that $y_{\mathcal{MF}}(\mathbf{X}_*) = y_{\mathcal{LF}}(\mathbf{X}_*) + y_{\delta}(\mathbf{X}_*)$ and $\sigma_{\mathcal{MF}}(\mathbf{X}_*) = \sigma_{\mathcal{HF}}(\mathbf{X}_*) = \sigma_{\delta}(\mathbf{X}_*)$. Fig. 4 illustrates a high fidelity and a multi-fidelity GP regression model from Eq. (11) with three different low fidelity active samples.

Fig. 4 is an illustration used to compare the performance of high fidelity and multi-fidelity GP regression models and demonstrate the motivation for the inter-model acquisition function. In Fig. 4(a), the next three optimal sampling locations are located using an acquisition function low fidelity GP regression model. Comparing Figs. 4(a) and 4(b) demonstrates that the first two low fidelity active samples have little impact on the mean of the multi-fidelity GP regression model. This is because the multi-fidelity GP regression model is approximate to the ground truth in these sampling locations so little improvement is made by taking these samples. The model is already relatively accurate despite having a large uncertainty at these locations. However, the third low fidelity sample has a large impact on the multi-fidelity GP regression model because the ground truth is farther away from the predicted mean. For this reason, the inter-model acquisition function in use for this study calculates the absolute difference between the predicted mean of the high and multi-fidelity GP regression models. This is referred to as the absolute difference inter-model acquisition function and is defined in Eq. (17). The high fidelity sample is selected at the location in the domain where the maximum absolute difference between the mean of the high and multi-fidelity GP model exists. This is chosen to capitalize on the exploration of the low fidelity sampling to identify regions where the high fidelity model is inaccurate. If this difference is the result of a divergence between the low and high fidelity simulations, then the $\delta(\mathbf{X}_*)$ GP model from Eqs. (10) and (11) is updated to account for this discrepancy to retain the accuracy of the multi-fidelity GP regression model. This allows the multi-fidelity GP regression model to provide greater opportunities to identify optimal locations for future high fidelity samples. This ultimately enables the multi-fidelity inter-model active sampling to outperform high fidelity active sampling.

$$
\begin{aligned}
q_{AD}(\mathbf{X}_*) &= |y_{\mathcal{HF}}(\mathbf{X}_*) - y_{\mathcal{MF}}(\mathbf{X}_*)| = |y_{\mathcal{HF}}(\mathbf{X}_*) - (y_{\mathcal{LF}}(\mathbf{X}_*) + y_{\delta}(\mathbf{X}_*))| \\
x_{\mathcal{HF}}^{*} &= \arg\max q_{AD}(\mathbf{X}_*) = \arg\max |y_{\mathcal{HF}}(\mathbf{X}_*) - y_{\mathcal{MF}}(\mathbf{X}_*)|
\end{aligned}
\tag{17}
$$

In summary, the inter-model acquisition function is used to determine the next optimal high fidelity sampling location by considering the statistics from different fidelity models. Because the low fidelity model can be sampled many times before sampling a high fidelity data point, the non-myopic characteristic of the acquisition function emerges. It considers how the low fidelity model changes as it iterates through many future low fidelity samples and uses this information to determine the location of the next high fidelity sample. This non-myopia allows the more robust exploration of the domain in the low fidelity regime before a high fidelity sample is taken. Extensively searching the low fidelity domain increases the likelihood of identifying regions with large model errors. These regions are likely to carryover into the high fidelity regime and provide an optimal sampling location where a high fidelity sample will provide large improvement to the model accuracy.

3.2. Non-Myopic Multi-Fidelity (NMMF) active learning algorithm

By combining the multi-fidelity GP regression framework with the non-myopic approach for active learning, we proceed with the formulation of a non-myopic multi-fidelity active learning algorithm. It consists of the following steps and the pseudo-code is listed in Algorithm 1:

1. Begin with a small number of high and low fidelity simulations to make initial data sets, i.e. $\mathcal{D}_{\mathcal{HF}}$ and $\mathcal{D}_{\mathcal{LF}}$. These high and low fidelity simulations are performed at the same $\mathbf{X}$ locations within the domain but result in different outputs, i.e. $\mathbf{y}_{\mathcal{HF}}$ and $\mathbf{y}_{\mathcal{LF}}$. These initial data sets are used to determine $\mathcal{D}_{\delta} = \{\mathbf{X}, \mathbf{y}_{\delta}\}$ from Eq. (15). Next, GP regression is performed on $\mathcal{D}_{\mathcal{HF}}, \mathcal{D}_{\mathcal{LF}}, \mathcal{D}_{\delta}$ to obtain $y_{\mathcal{LF}}$, $y_{\mathcal{HF}}$, y_{δ}, $\sigma_{\mathcal{LF}}$, and $\sigma_{\mathcal{HF}} = \sigma_{\delta}$ using Eqs. (12), (13), and (14).

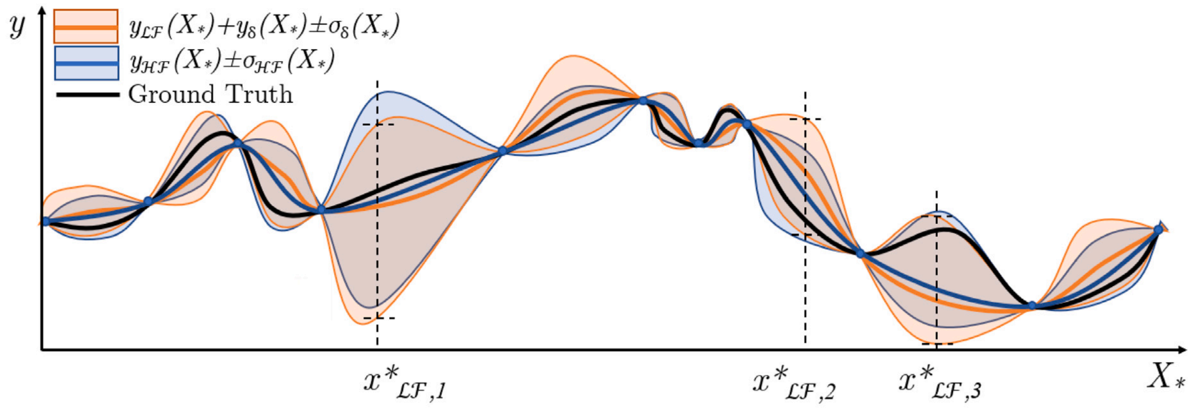

(a) Low Fidelity Active Sampling: The predicted mean error of the high (blue) and multi-fidelity (orange) GP regression model are shown. Active sampling is used to determine the next three low fidelity sampling locations.

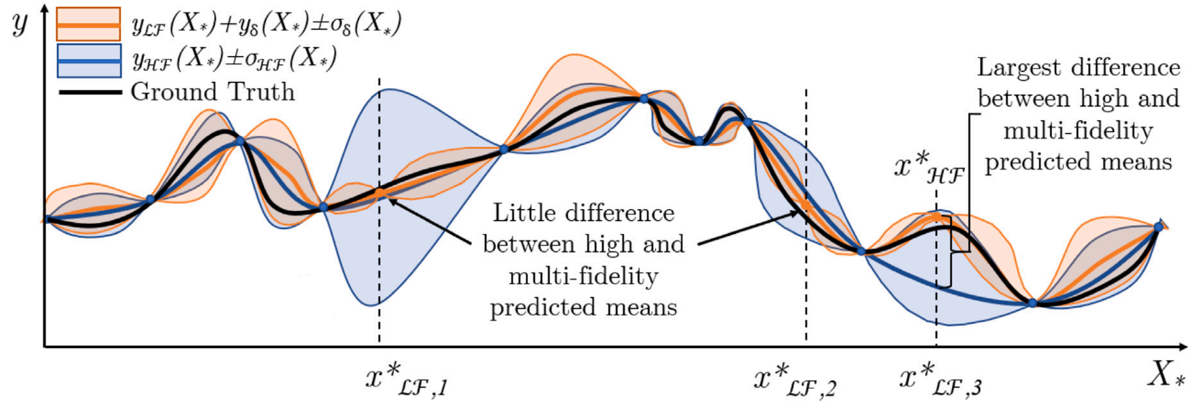

(b) Inter-Model Active Sampling: The next optimal high fidelity sampling location is determined by utilizing the statistics of the both the high fidelity GP regression model and the multi-fidelity model.

Fig. 4. Inter-model acquisition function: An example predicted mean and error of the high (blue) and multi-fidelity (orange) GP regression models are plotted against the ground truth data (black) that all the different fidelity models are attempting to replicate. The location of the next high fidelity sample is determined by considering the difference between the predicted mean of the high and multi-fidelity models. This optimal location is determined using the statistics of two different fidelity models.

2. Perform active learning to select an optimal sample from the low fidelity model $x^*_{\mathcal{LF}}$ using Eq. (8) and run the corresponding low fidelity simulation to obtain $y^*_{\mathcal{LF}}$. The uncertainty sampling acquisition function in Eq. (9) is used in this study due to its robustness, but other acquisition functions are acceptable. After the sample has been selected and simulated, GP regression is performed using Eq. (13) to find the new $y_{\mathcal{LF}}$ and $\sigma_{\mathcal{LF}}$. This low fidelity sampling is repeated for a set number of iterations j, which is a parameter set by the user. This search provides new information about the low fidelity GP regression model at many new points without having the cost of running multiple high fidelity simulations.
3. Select the high fidelity sample $x^*_{\mathcal{HF}}$ using Eq. (17) and perform the high fidelity simulation to obtain $y^*_{\mathcal{HF}}$ at this sample location. This inter-model acquisition function is non-myopic because it considers how the low fidelity model evolves through multiple samples and uses this information to select the high fidelity sampling location. Next, perform a low fidelity simulation at the location of the high fidelity sample and add it to the low fidelity data set $\mathcal{D}_{\mathcal{LF}}$.
4. Remove any low fidelity samples from the low fidelity data set $\mathcal{D}_{\mathcal{LF}}$ that are not at locations where high fidelity samples are also taken. The examples in this study removed these low fidelity samples in order to compare acquisition performance against other acquisition methods with the same size data sets in order to provide a fair comparison, rather than see model improvement due to larger data sets. While removing low fidelity samples may potentially result in a less accurate model, this is also a more robust approach because it prevents the low fidelity data set from becoming too large and ill-conditioned resulting in problematic inverse matrix operations in Eq. (13) during GP regression. However, this algorithm may be used without removing these low fidelity samples if the data set is small enough to allow accurate GP regression modeling. Next, use Eq. (15) to update $\mathcal{D}_\delta$ with the new high fidelity sample. Finally, perform GP regression on $\mathcal{D}_{\mathcal{HF}}, \mathcal{D}_{\mathcal{LF}}, \mathcal{D}_\delta$ to obtain $y_{\mathcal{LF}}$, $y_{\mathcal{HF}}$, y_δ, $\sigma_{\mathcal{LF}}$, and $\sigma_{\mathcal{HF}} = \sigma_\delta$ using Eqs. (12), (13), and (14).
5. Repeat steps 2 through 4 until the desired number of high fidelity samples is taken.

The pseudo-code in Algorithm 1 outlines the non-myopic multi-fidelity active learning algorithm for GP regression.

Algorithm 1 Non-Myopic Multi-Fidelity (NMMF) Active Learning

```
Input: $\mathcal{D}_{\mathcal{HF}} = \{X_{\mathcal{HF}}, \mathbf{y}_{\mathcal{HF}}\}, \mathcal{D}_{\mathcal{LF}} = \{X_{\mathcal{LF}}, \mathbf{y}_{\mathcal{LF}}\}, \mathcal{D}_{\delta} = \{\mathbf{X}_{\delta}, \mathbf{y}_{\delta}\}$ where $X_{\mathcal{LF}} = X_{\mathcal{HF}} = X_{\delta}$
Perform GP regression on $\mathcal{D}_{\mathcal{HF}}, \mathcal{D}_{\mathcal{LF}}, \mathcal{D}_{\delta}$ to obtain $y_{\mathcal{LF},0}(\mathbf{X}_*)$, $\sigma_{\mathcal{LF},0}(\mathbf{X}_*)$, $y_{\mathcal{HF},0}(\mathbf{X}_*)$, $\sigma_{\mathcal{HF},0}(\mathbf{X}_*)$,
    $y_{\delta,0}(\mathbf{X}_*)$, $\sigma_{\delta,0}(\mathbf{X}_*)$; equations ((12), (13), (14))
For $i = 1$ to $m$
    For $j = 1$ to $n$
        Select low fidelity location $x^*_{\mathcal{LF},j} = arg\ min\ q_{US}$ $(\mathbf{X}_*|\sigma_{\mathcal{LF},j-1}(\mathbf{X}_*))$;
            equations ((8), (9))
        Run low fidelity simulation at $x^*_{\mathcal{LF},j}$ to obtain $y^*_{\mathcal{LF},j}$
        Temporarily augment data set $\mathcal{D}_{\mathcal{LF},j} = \{(\mathbf{X}_{\mathcal{LF},j-1}, \mathbf{y}_{\mathcal{LF},j-1}) \cup (x^*_{\mathcal{LF},j}, y^*_{\mathcal{LF},j})\}$
            until $x^*_{\mathcal{HF},i}$ is found
        Perform GP regression on $\mathcal{D}_{\mathcal{LF},j}$ to obtain $y_{\mathcal{LF},j}(\mathbf{X}_*), \sigma_{\mathcal{LF},j}(\mathbf{X}_*)$; equation (13)
    End For
    Select high fidelity location $x^*_{\mathcal{HF},i} = arg\ max\ q_{AD}(\mathbf{X}_*|y_{\mathcal{HF}}(\mathbf{X}_*), y_{\mathcal{LF}}(\mathbf{X}_*), y_{\delta}(\mathbf{X}_*))$;
        equation (17)
    Run high fidelity simulation at $x^*_{\mathcal{HF},i}$ to obtain $y^*_{\mathcal{HF},i}$
    Augment data set $\mathcal{D}_{\mathcal{HF},i} = \{(\mathbf{X}_{\mathcal{HF},i-1}, \mathbf{y}_{\mathcal{HF},i-1}) \cup (x^*_{\mathcal{HF},i}, y^*_{\mathcal{HF},i})\}$
    Restore low fidelity data set $\mathcal{D}_{\mathcal{LF}}$ to condition before augmented with $x^*_{\mathcal{LF},j}, y^*_{\mathcal{LF},j}$, i.e. $\mathcal{D}_{\mathcal{LF},i-1}$
    Run low fidelity simulation at $x^*_{\mathcal{LF},i} = x^*_{\mathcal{HF},i}$ to obtain $y^*_{\mathcal{LF},i}$
    Augment data sets $\mathcal{D}_{\mathcal{LF},i} = \{(\mathbf{X}_{\mathcal{LF},i-1}, \mathbf{y}_{\mathcal{LF},i-1}) \cup (x^*_{\mathcal{LF},i}, y^*_{\mathcal{LF},i})\}$, and
        $\mathcal{D}_{\delta,i} = \{(\mathbf{X}_{\delta,i-1}, \mathbf{y}_{\delta,i-1}) \cup (x^*_{\mathcal{LF},i}, y^*_{\mathcal{HF},i} - y^*_{\mathcal{LF},i})\}$; equation (15)
    Perform GP regression on $\mathcal{D}_{\mathcal{HF},i}, \mathcal{D}_{\mathcal{LF},i}, \mathcal{D}_{\delta,i}$ to obtain $y_{\mathcal{LF},i}(\mathbf{X}_*)$, $\sigma_{\mathcal{LF},i}(\mathbf{X}_*)$, $y_{\mathcal{HF},i}(\mathbf{X}_*)$,
        $\sigma_{\mathcal{HF},i}(\mathbf{X}_*)$, $y_{\delta,i}(\mathbf{X}_*)$, $\sigma_{\delta,i}(\mathbf{X}_*)$; equations ((12), (13), (14))
End For
```

Overall, this new non-myopic multi-fidelity framework utilizes the low cost of the low fidelity simulations to explore the domain, as well as optimally selected high fidelity simulations to improve the model accuracy. This allows for GP regression models to become more accurate while reducing the computational cost of running high fidelity simulations.

3.3. Advantages of multi-fidelity Gaussian process regression model

While the multi-fidelity GP regression model serves a vital role in the active learning process, there are additional benefits that come from using this approach. Because this multi-fidelity GP model is used to exploit the relationship between the high fidelity and low fidelity simulators, modeling differences between the simulators could help developers to better understand the limitations of low fidelity simulators. While it is necessary to have prior knowledge of the low and high fidelity simulator performance during development, this approach provides quantifiable differences and errors of the different fidelity models which may prove valuable. There may be portions of the input space in which the low fidelity model is suitable for many purposes. The multi-fidelity GP model helps quantify the accuracy of the low fidelity model with respect to the high fidelity model. Additionally, the results of the multi-fidelity GP model could be integrated directly into the low fidelity simulators to improve their accuracy.

4. Evaluation of NMMF active learning algorithm

To assess the performance of the NMMF active learning algorithm compared to other state of the art algorithms, a large number of high fidelity simulations needs to be performed. For this reason, we first demonstrate its advantages on some test problems and then we apply it to CFD problems. Specifically, the performance of the developed algorithm is compared to that of the traditional myopic multi-fidelity sampling method, as well as the standard sampling method using the uncertainty sampling acquisition function for the high fidelity model.

Two different prototype problems are selected in a multi-fidelity setup with a number of dimensions close to that of the UUV and submarine hydrodynamics problem. For both of the problems in this section, the number of low fidelity samples that are performed before selecting the high fidelity sampling location is held constant at 10 for consistency. However, this is a parameter that may be adjusted for other applications based on the computational cost of the low fidelity search and the dimensionality of the domain. The error used to evaluate the accuracy of the surrogates is the Mean Absolute Percentage Error (MAPE). This is chosen because it normalizes the error, rather than looking at absolutes error alone. The MAPE is defined in the following equation in terms of the predicted quantity, y_p, and its exact value y_e:

$$MAPE = \frac{1}{n}\sum_{i=1}^{n}\left|\frac{y_{p,i} - y_{e,i}}{y_{e,i}}\right| \tag{18}$$

4.1. Three DOF trebuchet with a hinged counterweight and sling

We first consider the simulation of projectile range from a three degree of freedom trebuchet with a hinged counterweight and sling (Constans, 2013; Siano, 2013; Rutan and Wieczorek, 2005). Fig. 5 illustrates the mechanical system of the simulation.

Using Lagrangian mechanics, the equations of motion outlined in Eq. (19) are derived to simulate the motion of the trebuchet using the variables defined in Fig. 5. These equations of motion are coupled and highly non-linear. These are the types of problems for which surrogate models are often created.

$$\begin{bmatrix} m_1 l_1^2 + m_2 l_2^2 + m_{arm} l_{arm}^2 + I_{arm} & m_1 l_1 l_4 \cos(\theta - \phi) & -m_2 l_2 l_3 \cos(\theta - \phi) \\ m_1 l_1 l_4 \cos(\theta - \phi) & m_1 l_4^2 & 0 \\ -m_2 l_2 l_3 \cos(\theta - \phi) & 0 & m_2 l_3^2 \end{bmatrix} \times \begin{bmatrix} \ddot{\theta} \\ \ddot{\phi} \\ \ddot{\psi} \end{bmatrix} = \begin{bmatrix} -m_1 l_1 l_4 \dot{\phi}^2 \sin(\theta - \phi) + m_2 l_2 l_3 \dot{\psi}^2 \sin(\theta - \phi) - (m_1 l_1 - m_2 l_2 - m_{arm} l_{arm}) g \cos(\theta) \\ m_1 l_1 l_4 \dot{\theta}^2 \sin(\theta - \phi) - m_1 l_4 g \cos(\phi) \\ m_2 l_2 l_3 \dot{\theta}^2 \sin(\theta - \phi) - m_2 l_3 g \cos(\psi) \end{bmatrix} \tag{19}$$

where $m_{arm} = f(l_1, l_2, constants)$, $l_{arm} = f(m_{arm}, l_1, l_2, constants)$, and $I_{arm} = f(m_{arm}, l_1, l_2, constants)$.

The initial conditions in use to solve the system of equations are listed below:

$$\theta_0 = \sin^{-1}\left(\frac{h_0}{l_2}\right), \ \phi_0 = \frac{-\pi}{2}, \ \psi_0 = 0, \ \dot{\theta}_0 = 0, \ \dot{\phi}_0 = 0, \ \dot{\psi}_0 = 0 \tag{20}$$

The projectile is released at a constant launch hook angle β. The launch hook angle is the angle between the trebuchet arm l_2 and sling l_3. After the projectile is released, the range of the projectile is determined using standard Newtonian projectile motion physics which neglects air resistance.

These equations of motion have the potential to allow for a higher dimension domain by allowing more parameters to vary, like the launch hook angle β or other trebuchet arm moment of inertia parameters like material density or thickness of the arm. Likewise, the domain could be reduced by fixing certain input variables to a constant value. The domain for this problem is selected to be six-dimensional and the range

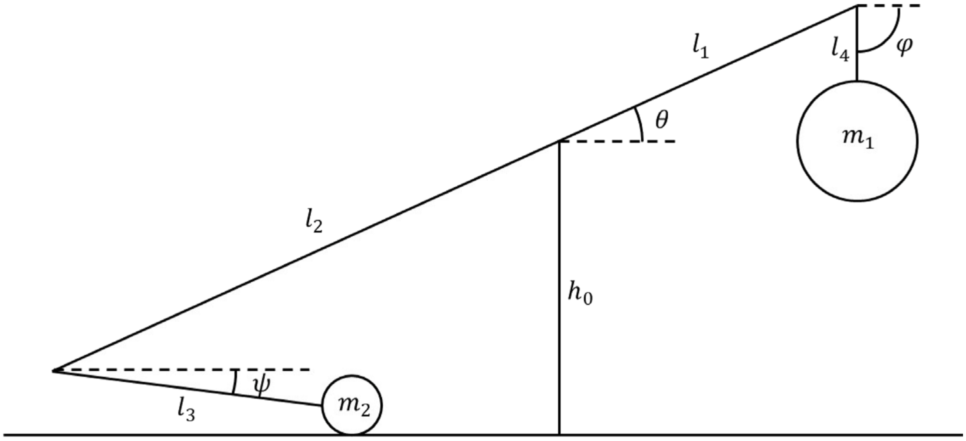

Fig. 5. Three degree of freedom trebuchet with a hinged counterweight (m_1) and projectile (m_2) mounted in a sling.

of the various input variables is as follows:

$$\begin{aligned} l_1 &\in [0.5, 1.5] \\ l_2 &\in [3.5, 4.5] \\ l_3 &\in [3.0, 4.0] \\ l_4 &\in [0.1, 1.0] \\ h_0 &\in [3.0, 3.5] \\ m_1 &\in [40, 400] \end{aligned} \tag{21}$$

A simpler two degree of freedom simulation known as a trebuchet with a fixed counterweight and sling is used for the low fidelity model. Unlike the previous trebuchet model, the counterweight is not hinged and is mounted directly on the end of the trebuchet rotating arm. Because this two degree of freedom trebuchet has the same potential as the previous trebuchet model, the performance is similar except that the low fidelity model cannot capture the efficiency effects that are influenced by the hinged counterweight. Fixing the counterweight simplifies the equations of motion by removing the influence of the l_4 and ϕ variables which reduces the computational cost.

Fig. 6 shows the performance of the different sampling methods on the three degree of freedom trebuchet problem. The entire process of creating a new surrogate model from 60 high fidelity active samples is repeated 100 times. This is performed in order to reduce the variation between repetitions to better assess the accuracy of the sampling method. Also, the same number of high fidelity samples is taken for each sampling method to allow for fair comparison of the sampling techniques.

Overall, the NMMF sampling algorithm outperforms both the myopic multi-fidelity and standard high fidelity algorithms. This sampling method produces a more accurate model with fewer high-fidelity experiments than the other sampling methods, although the benefits, in this case, are not substantial. The fact that the myopic multi-fidelity sampling algorithm outperforms the high fidelity sampling method is also consistent with other results in literature (Grassi et al., 2020; Takeno et al., 2020).

4.2. Borehole function

The borehole function is an eight-dimensional highly non-linear equation developed by Harper and Gupta (1983). This equation is used to determine the volumetric flow rate through a borehole that is drilled through an upper aquifer, a nuclear waste repository, and into a lower aquifer. This function has been used in literature to evaluate the performance of computer models. Xiong also developed a low fidelity approximation of this model which enables the borehole function to also evaluate multi-fidelity models (Xiong et al., 2013). The multi-fidelity borehole function, listed in Eqs. (22) and (23), is used to evaluate the performance of the non-myopic multi-fidelity sampling algorithm.

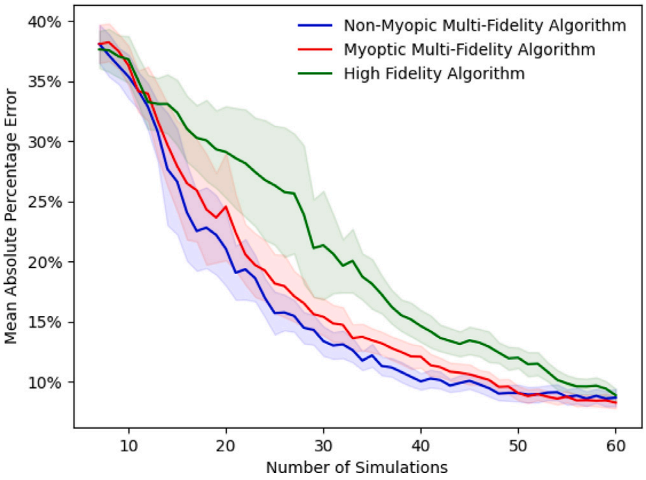

Fig. 6. Comparison of non-myopic multi-fidelity active learning algorithm against other active sampling algorithms on the three degree of freedom trebuchet. The error bands indicate one half of the median absolute deviation.

$$y_{\mathcal{HF}}(x) = \frac{2\pi T_u(H_u - H_l)}{\ln(r/r_w)} \left(1 + \frac{2LT_u}{\ln(r/r_w) r_w^2 K_w} + \frac{T_u}{T_l}\right)^{-1} \tag{22}$$

$$y_{\mathcal{LF}}(x) = \frac{5T_u(H_u - H_l)}{\ln(r/r_w)} \left(1.5 + \frac{2LT_u}{\ln(r/r_w) r_w^2 K_w} + \frac{T_u}{T_l}\right)^{-1} \tag{23}$$

Eq. (24) lists the domain of the various input variables.

$$\begin{aligned} r_w &\in [0.05, 0.15] \\ r &\in [100, 50000] \\ T_u &\in [63070, 115600] \\ H_u &\in [990, 1110] \\ T_l &\in [63.1, 116] \\ H_l &\in [700, 820] \\ L &\in [1120, 1680] \\ K_w &\in [9855, 12045] \end{aligned} \tag{24}$$

The different GP sampling methods are evaluated on the borehole function. Each surrogate model takes 100 high fidelity samples and repeats this process 450 different times in order to reduce the variance of the results of the different surrogates. Fig. 7 shows how each method performs on the borehole function test case.

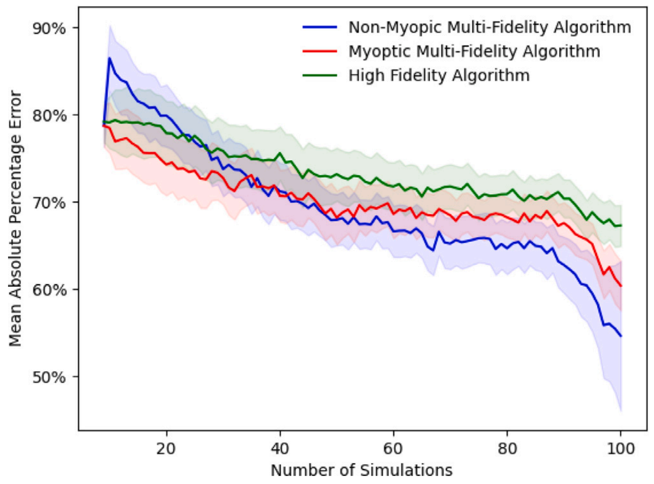

Fig. 7. Comparison of non-myopic multi-fidelity active learning algorithm against other active sampling algorithms on the borehole function. The error bands indicate one half of the median absolute deviation.

The NMMF sampling method is able to produce the lowest model error in the majority of the solution space. Initially, this method has the highest error, but it rapidly improves to the most accurate sampling scheme, approximately after 30 to 40 simulations are conducted. This is likely because the low and high fidelity models have a larger difference than in the other test cases. This means that the initial high fidelity samples are likely used to quantify the difference $\delta(\mathbf{X}_*)$ (Eqs. (10) and (11)) between the high and low fidelity models, rather than better explore the domain. Once this difference is well explored and quantified, the exploratory benefits of the NMMF algorithm quickly outperform the other two sampling methods.

5. Adaptations for multi-dimensional outputs

The considered prototype problems demonstrate the effectiveness of the NMMF active learning algorithm in setups where the output is a scalar quantity. However, for the submarine and UUV hydrodynamic interaction problem, the surrogate model has a vector output, which includes the surge force, sway force, and yawing moment experienced by the UUV. One can address this issue by simply building three separate surrogate models, one for each output. However, having multiple outputs creates a new obstacle. When a high fidelity CFD simulation is run at a single location in the domain, all three outputs are determined. The acquisition functions so far have been for a single output and they need to be modified to account for multiple outputs. The best way to make these modifications is explored.

Three different methods are considered as options to determine the optimal sampling location for the multiple outputs. The first is a “round robin” method, meaning that the output for which the optimal point is selected is alternated between all the outputs. The number of outputs of the surrogate is denoted as k. Let σ_i^2 denote each one of the three different surrogate output variances or epistemic uncertainties where $i = 1, \ldots, k$. Eq. (25) shows the “round robin” method in which the sampling location is selected by alternating which output is used for the acquisition function over the span of all n samples.

$$x^*_{j+1} = \arg\max q_{US}\left(x|\sigma_i\right) \;\text{ for } i = j - 1(\,mod\ k) + 1. \tag{25}$$

The second method is the “maximum variance” method. This approach begins by computing the optimal sampling location x_i' for each output individually. Next, the GP model is used to predict the epistemic variance at each location $\sigma_i^2(x_i')$. This is then normalized by the actual variance of the output data for each output $\sigma_{y,i}^2$. Lastly, the sampling location with the largest normalized variance is selected because this is the theorized location in which a sample could best reduce the uncertainty of the multiple outputs. Eq. (26) denotes the “maximum variance” method.

$$x^*_{j+1} = \arg\max \left(\frac{\sigma_i^2(x_i')}{\sigma_{y,i}^2}\right) \;\text{ for } i = 1, \ldots, k,$$
$$\text{where}\quad x_i' = \arg\max q_{US}(x|\sigma_i^2) \;\text{ and }\; \sigma_{y,i}^2 = \frac{1}{j}\sum_{l=1}^{j}\left(y_{i,l} - \bar{y}_i\right)^2. \tag{26}$$

The third method under consideration is called the “weighted” method. This approach looks for an optimal sampling location by assessing the multiple outputs as a whole rather than individually. Specifically, the statistics of the individual outputs are combined based on a weight factor into a single weighted variance σ_w^2 to be used with the uncertainty sampling acquisition function. The weight used for each output is the inverse of its training data variance for that given output. This is used as the weight in order to try and normalize the different output variances before they are combined. If they are not normalized, then the variance of one output could dominate the weighted variance, even if it has a low epistemic uncertainty. This could happen because the outputs are not normalized so outputs with larger values would have a larger impact on the weighted variance. Once these individual variances are combined into a single weighted variance, the optimal sampling location is selected using the following acquisition function:

$$x^*_{j+1} = \arg\max q_{US}(x|\sigma_w^2(x)), \quad \text{where} \quad \sigma_w^2(x) = \sum_{i=1}^{k}\frac{\sigma_i^2(x)}{\sigma_{y,i}^2} \tag{27}$$

An example problem with three outputs y_1, y_2, and y_3 is used to evaluate these different multiple output sampling methods. The Park 1, Park 2, and Colville functions listed as Eqs. (28), (29), and (30) are used as the three surrogate outputs (Surjanovic and Bingham, 2013). The domain of the input space is $x_i \in [0.1, 1]$ for all $i = 1, 2, 3, 4$.

$$y_1(x) = \frac{2}{3}e^{x_1+x_2} - x_4\sin(x_3) + x_3 \tag{28}$$

$$y_2(x) = \frac{x_1}{2}\left[\sqrt{1 + (x_2 + x_3^2)\frac{x_4}{x_1^2}} - 1\right] + (x_1 + 3x_4)e^{1+\sin(x_3)} \tag{29}$$

$$\begin{aligned} y_3(x) = {} & 100(x_1^2 - x_2)^2 + (x_1 - 1)^2 + (x_3 - 1)^2 + 90(x_3^2 - x_4)^2 \\ & + 10.1((x_2 - 1)^2 + (x_4 - 1)^2) + 19.8(x_2 - 1)(x_4 - 1) \end{aligned} \tag{30}$$

The various multiple output sampling methods are repeated 100 times to ensure the results are consistent. Fig. 8 shows the performance of each sampling method.

The “maximum variance” method slightly outperforms the other two sampling methods. This is true when looking at each output individually and also when looking at the average MAPE of all three outputs. The only portion of the solution space in which the “maximum variance” criterion did not outperform the other two methods is in the early stages of the sampling with less than 20 samples for y_1. The “round robin” method allocates optimal samples to this output despite it having the smallest error while the “maximum variance” method allocates optimal samples for the outputs with larger errors. This allows the “round robin” method to temporarily outperform the “maximum variance” method for y_1. However, the “maximum variance” method is able to quickly catch up and outperform the “round robin” method for this output. The “weighted” method underperformed the other two methods. To this end, the “maximum variance” criterion is selected as the multiple output sampling method for the UUV and submarine hydrodynamic interactions problem.

6. UUV and submarine hydrodynamic interaction

The NMMF active learning GP regression model with the “maximum variance” multiple output selection criterion is used to model the hydrodynamic interactions between a UUV and submarine. For this

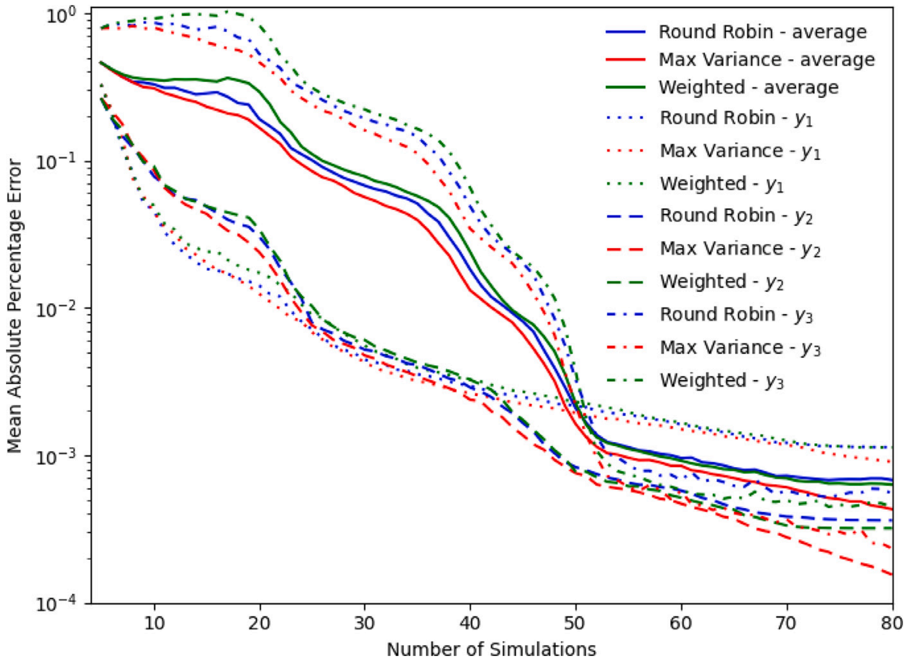

Fig. 8. Comparison of the "round robin", "maximum variance", and "weighted" multiple output active sampling methods for three test cases.

study, the high fidelity model is a commercial CFD solver known as Star-CCM+ that iteratively solves the Reynolds-averaged Navier–Stokes equations in order to determine the forces and moments on the UUV. Additionally, the low fidelity model is a potential flow solver known as FS-Flow (Anon, 2018). This tool uses simplified physics which neglects viscosity, skin friction, boundary layer development, flow separation, and leads to the d'Alembert paradox which predicts zero drag on a UUV moving at constant velocity (Newman, 2017). In order to overcome these physical limitations, this potential flow solver is supplemented with a simple parametric model to help predict the effects of viscosity on the moving body. FS-Flow uses the panel method to resolve the flow around a moving body and supplements the solution with one of four different viscous correlation lines. The frictional resistance can be estimated using the International Towing Tank Conference (ITTC) 57, Hughes, Grigson, or Katsui viscous correlation lines (Anon, 2018). The ITTC-57 correction line is used for this study.

6.1. Experimental design

In order for the surrogate to be useful in modeling launch and recovery operations, the surrogate has to accurately predict the hydrodynamic interaction forces and moments on the UUV. For simplicity, the only three degrees of freedom for the UUV are surge, sway, and yaw. This means that the output of the surrogate is chosen to be the well defined surge, X', sway, Y', and yaw, N', coefficients of the UUV (Fossen, 2011; Gertler and Hagen, 1967). The UUV position, heading angle, speed, and size all have an impact on these output variables, so these parameters are broken down into six input variables.

The UUV position is defined by a longitudinal separation ratio, R_{Long}, and a lateral separation ratio, R_{Lat}. These parameters are the longitudinal and lateral distance between the centers of buoyancy of the two vehicles normalized by the length of the submarine. The heading angle, ϕ, is the angle between the body of revolution axes of the two vehicles with a positive heading angle corresponding to the bow of the UUV pointing away from the submarine. Fig. 9 and Eqs. (31) and (32) illustrate the longitudinal separation ratio, lateral separation ratio, and heading angle.

$$R_{Long} = \frac{x_{Dist}}{L_{Sub}} \tag{31}$$

Table 1
Input variables and domains for hydrodynamic interaction reduced order model.

Symbol	Description	Units	Bounds
R_{Long}	Longitudinal separation ratio	None	[−0.7,0.7]
R_{Lat}	Lateral separation ratio	None	[0.059,0.105]
U	Speed	Knots	[2,5]
ϕ	Heading angle	Degrees	[−2,2]
D_{Sub}/D_{UUV}	Submarine to UUV diameter ratio	None	[5,50]
L/D_{UUV}	UUV length to diameter ratio	None	[4.3,13]

$$R_{Lat} = \frac{y_{Dist}}{L_{Sub}} \tag{32}$$

Likewise, the UUV length and diameter are non-dimensionalized using ratios. Because the submarine diameter is fixed, the submarine to UUV diameter ratio is selected as a non-dimensional parameter to represent various diameters of the UUV. Lastly, the UUV length to diameter ratio is then used to account for the different lengths of UUV. Table 1 summarizes each of the six different input variables with their accompanying units and bounds.

As certain bounds of the domain in Table 1 are increased, the uncertainty of the high fidelity solutions in some parts of the domain becomes very large. For example, as the heading angle of the UUV becomes large, the sway created by the flow incident on the UUV at a large angle dominates the hydrodynamic interactions due to operating near the submarine. This reduces the ability to model the hydrodynamics. This is also an unlike operating condition of the UUV. Hence, there is a trade-off between exploration and accuracy. The bounds of this domain are selected to capture the wide range of input variables necessary to simulate UUV motion while being restrictive enough to produce accurate results. While this domain considers this trade-off, additional constraints are established to exclude certain unrealistic parts of the domain based on input variable interactions. For example, larger diameter UUVs tend to be shorter while smaller diameter UUVs tend to be longer. Two constraints are created based on real-world UUV measurements which ignore the combination of UUV lengths and diameters that are infeasible. Additionally, the relationship between lateral distance from the submarine and the UUV diameter is constrained. This enables the center of buoyancy of the small diameter UUVs to get closer

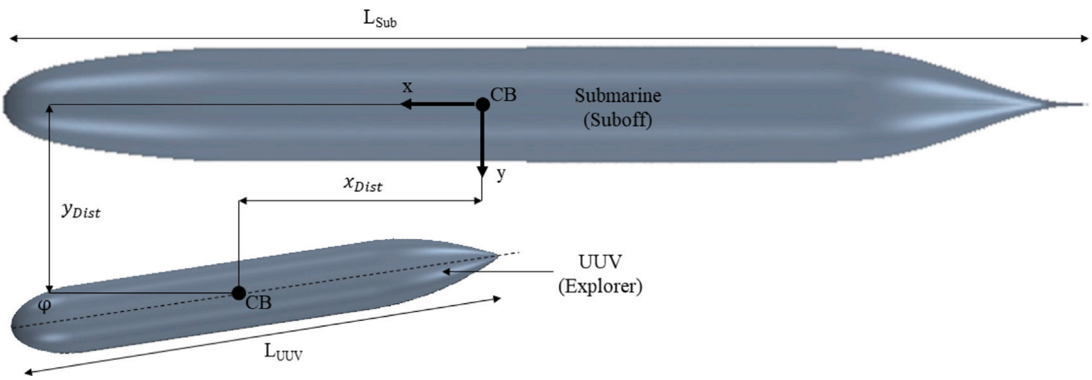

Fig. 9. Geometry and orientation of the submarine and UUV hydrodynamic interaction experimental setup.

to the submarine. The center of buoyancy of a larger diameter UUV in this region would result in a collision between the vehicles. Likewise, UUVs are constrained, based on diameter, to make sure they are not so far away as to avoid any hydrodynamic interactions. These constraints are formalized as follows using the input variables defined in Table 1:

1. The following non-dimensional constraint is established to ensure that the two vehicles maintain a minimum clearance of 0.05 meters regardless of the UUV size, heading angle, or position.

$$8.575R_{Lat} - 0.5\left(\frac{D_{Sub}}{D_{UUV}}\right)^{-1} - 9.425 \cdot 10^{-3}\phi\left(\frac{D_{Sub}}{D_{UUV}}\right)^{-1} \times (L/D_{UUV}) - 0.5048 \geq 0 \tag{33}$$

2. This non-dimensional constraint maintains the distance between the centers of buoyancy of the two vehicles y_{Dist} to be less than or equal to $2D_{UUV} + D_{Sub}/2$ in order to ensure the vehicles are close enough to experience large hydrodynamic interactions.

$$-8.575R_{Lat} + 2\left(\frac{D_{Sub}}{D_{UUV}}\right)^{-1} + 0.5 \geq 0 \tag{34}$$

3. Not all combinations of UUV lengths and diameters within the domain are feasible based on the dimensions of 15 commercially available UUVs. The following non-dimensional constraint eliminates the UUVs that are too short for their given diameter.

$$65.44\left(\frac{D_{Sub}}{D_{UUV}}\right)^{-1} + (L/D_{UUV}) - 8 \geq 0 \tag{35}$$

4. Likewise, the following non-dimensional constraint eliminates the UUVs that are too long for their given diameter.

$$-58.81\left(\frac{D_{Sub}}{D_{UUV}}\right)^{-1} - (L/D_{UUV}) + 17 \geq 0 \tag{36}$$

The NMMF active search algorithm was iterated until 100 high fidelity simulations were performed. At this point, the model had converged because each new high fidelity simulation provided little change to the output of the surrogate model for a set of test input data.

6.2. *Computational fluid dynamics*

The Defense Advanced Research Projects Agency (DARPA) SUBOFF model is used as the geometric model for the submarine hull while the International Submarine Engineering (ISE) Explorer is used for the UUV hull (Groves et al., 1989; Explorer AUV, 2020). In accordance with ITTC guidelines, the domain of the CFD simulation has at least one submarine length of clearance between the domain edges and the front of the vehicles. The aft end of the vehicles has three submarine lengths of clearance to the end of the domain (Practical Guidelines, 2014). The domain is made symmetrical along the plane that intersects the axes of the two vehicles and a symmetrical boundary layer condition is applied along this plane. This allows the domain to be half the size without compromising accuracy which greatly reduces the computational resources needed for the study.

The CFD simulations use an unstructured polyhedral overset mesh because it more easily accommodates mesh deformation and restructuring as the UUV is re-positioned between simulations (Leong, 2014). While the number of cells varies between simulations, the number of cells is typically between one and two million which is high enough to provide mesh independence (Moonesun et al., 2015).

According to the ITTC, the $k-\epsilon$ and $k-\omega$ turbulence models are by far the most common models that are applied to ship hydrodynamics and have consistently provided accurate predictions (Practical Guidelines, 2014). For this simulation, the $k-\omega$ turbulence model is selected because it is more accurate in adverse pressure gradients like those experienced on the stern of the model (Practical Guidelines, 2014; Menter, 1994). The total boundary layer thickness is calculated using the Prandtl's turbulent boundary layer thickness over a flat plate or $0.16L/Re_L^{1/7}$ (Leong et al., 2013). This boundary layer mesh uses prism layers with an expansion ratio of 1.2. The number of prism layers on the submarine and UUV are large enough to ensure that the non-dimensional wall distance y^+ values are less than one. This CFD simulation setup is in accordance with ITTC procedures (Practical Guidelines, 2014).

Once the CFD simulation setup is established, the next step is to validate if the CFD simulations are able to accurately predict real-world results. Submarine and UUV hydrodynamic interactions are very challenging to capture in experiments using tow tank experiments. This is because in order to maintain similitude between vehicle sizes, the UUV models become too small to allow for accurate measurements. However, Leong performed a series of tow tank experiments with a UUV that had a diameter of about 44.7% of the diameter of the submarine (Leong, 2014). While UUVs of this size are much too large to be considered for actual launch and recovery operations, these real-world experiments are used to validate the CFD setup. Fig. 10 compares the surge, sway, and yaw coefficients of the UUV for the CFD and tow tank experiments performed by Leong.

Fig. 10 shows that the CFD is able to predict all of the surge, sway, and yaw coefficients within the uncertainty of the tow tank experiments in all of the possible UUV locations. The UUV experiences large oscillations in sway and yaw, but the CFD is able to accurately capture these complex real-world hydrodynamic interactions.

6.3. *Results*

This experimental setup has six input parameters. There is no straightforward way to illustrate a six-dimensional parameter space, but to help visualize the results, a series of two-dimensional plots are

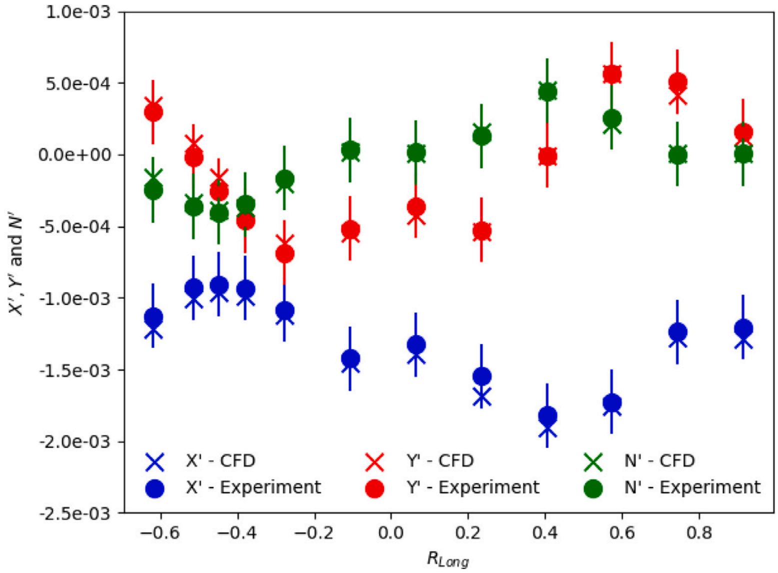

Fig. 10. Comparison of the CFD simulated surge, sway, and yaw force and moment coefficients at various longitudinal positions against the validated tow tank experiments by Leong (2014). All CFD simulated results are within the margin of error of the tow tank results.

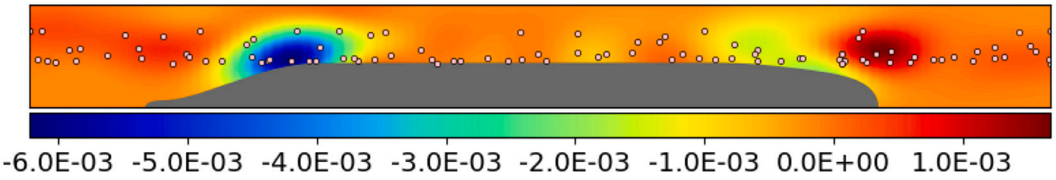

(a) Colormap of sway coefficient Y' at various locations around the submarine at a fixed $U = 3.5$ knots, $\phi = 0°$, $D_{Sub}/D_{UUV} = 10$, and $L/D_{UUV} = 8$. Regions around the bow of the submarine push the UUV away from the submarine while regions around the stern of the submarine pull the UUV toward the submarine.

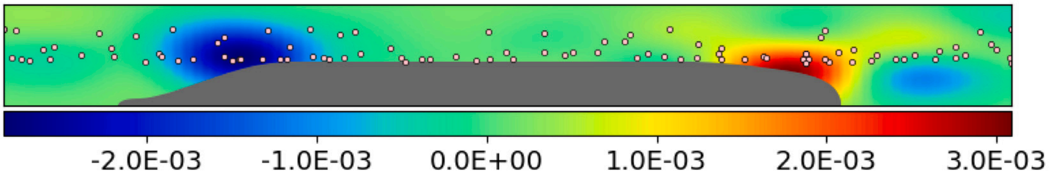

(b) Colormap of yaw coefficient N' at various locations around the submarine at a fixed $U = 3.5$ knots, $\phi = 0°$, $D_{Sub}/D_{UUV} = 10$, and $L/D_{UUV} = 8$. Regions around the bow of the submarine rotate the bow of the UUV away from the submarine while regions around the stern of the submarine rotate the UUV bow toward the submarine.

Fig. 11. Colormaps of the hydrodynamic interaction sway and yaw coefficients Y' and N' at different lateral and longitudinal positions with respect to the submarine. The dots represent the locations selected using the NMMF algorithm to perform a high fidelity CFD simulation.

generated while keeping the other four input dimensions constant. This allows the impact of each dimension to be assessed while also displaying some interactions between input variables.

Fig. 11 shows how the sway and yaw coefficients for the UUV vary as the UUV is in different lateral and longitudinal positions from the submarine. A positive sway coefficient pushes the UUV away from the submarine and a positive yaw moment causes the bow of the UUV to be rotated away from the submarine.

Each high fidelity CFD simulation is represented as a dot in Fig. 11. The domain is constrained such that the UUV will not be positioned directly in front of or behind the submarine in order to avoid the risk of a collision. This figure illustrates how there are large sway and yaw oscillations as a UUV changes its position longitudinally along the submarine. Near the bow of the submarine, the UUV experiences a sway and yaw force and moment that push the vehicle away and cause the UUV bow to rotate away from the submarine. However, near the stern of the submarine, the UUV is pulled toward and the UUV bow is rotated toward the submarine. The magnitude of these forces and moments decreases as the UUV is positioned laterally farther from the submarine. The oscillations in sway and yaw based on UUV location that are captured by this surrogate model are observed in tow tank experiments between a model submarine and UUV (Leong, 2014). However, these tow tank experiments are greatly limited in the size of the UUV that they can evaluate. In order to have similitude of the

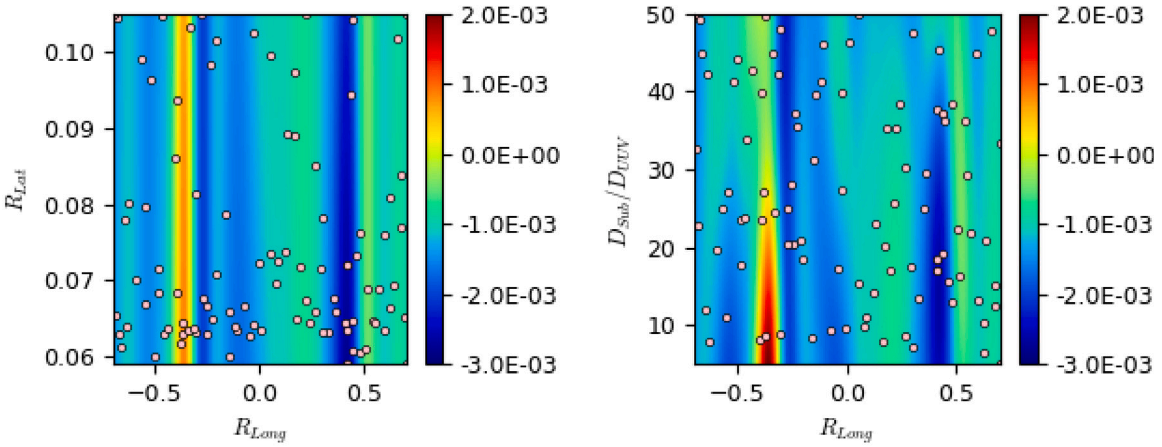

(a) Surge coefficient X' at various R_{Lat} and R_{Long} locations around the submarine at a fixed $U = 3.5$ knots, $\phi = 0°$, $D_{Sub}/D_{UUV} = 20$, and $L/D_{UUV} = 8$. Near the stern of the submarine, the reduced order model predicts a positive surge experienced by the UUV.

(b) Surge coefficient X' at various $D_{Sub/D_{UUV}}$ and R_{Long} locations around the submarine at a fixed $R_{Lat} = 0.08$, $U = 3.5$ knots, $\phi = 0°$, and $L/D_{UUV} = 8$. The reduced order model predicts the positive surge experiences near the stern of the submarine decreases for smaller diameter UUVs.

Fig. 12. UUV hydrodynamic interaction surge coefficient X' at various longitudinal separation ratios R_{Long} from the submarine.

diameter ratios between the real world vehicles, the model UUV would have to be too small to capture any accurate experimental data of the hydrodynamic interactions.

These large sway and yaw coefficients with steep gradients near the bow and stern of the submarine provide an obstacle for the launch and recovery of UUVs from submarines. Accurately modeling these forces and moments and incorporating them into the UUV control and autonomy systems could enable UUVs to predict these large hydrodynamic interactions and accurately navigate through these regions. Another option would be to develop launch and recovery architectures that avoid these regions altogether. This surrogate model could also be used to establish operating envelopes. These are regions in which the UUV should not operate in order to avoid forces or moments large enough to interfere with launch and recovery operations.

The surge force coefficient also experiences unique hydrodynamic interactions near the bow and stern of the submarine. Fig. 12 shows how the surge force coefficient varies along the length of the submarine.

Fig. 12 shows that the UUV experiences a substantial drop in the surge that opposes forward UUV motion near $R_{Long} \approx -0.4$. This phenomenon occurs when the UUV is located just aft of the parallel mid-body at the forward part of the submarine afterbody. In fact, this hydrodynamic interaction causes the surge force to become positive. This means that this hydrodynamic interaction overcomes the drag of the vehicle and would cause it to accelerate forward, even with no thrust from the UUV propeller. There is a low pressure region and the end of the parallel mid-body of the submarine as it transitions to the stern. There is also a high pressure region farther down the stern of the submarine. The UUV experiences this positive surge when it encounters the steep pressure gradient between these two regions. Also, as the fluid flows along the stern of the submarine and passes the bow of the UUV, it accelerates between the two vehicles due to the flow restriction. This Bernoulli effect causes an additional drop in pressure. The drop in pressure near the bow of the UUV also contributes to the drop in surge and causes the UUV to get pulled forward. Additionally, the flow around the stern of the submarine meets the UUV at an angle that causes a large lift. This lift is perpendicular to the flow and causes the resultant total force vector to have a component in the forward direction of the UUV. Fig. 13 summarizes this complex interaction.

This specific hydrodynamic interaction could make UUV launch and recovery operations particularly challenging because it is so far outside of the normal UUV operating window. Fig. 12(b) shows that the magnitude of this hydrodynamic interaction decreases as the diameter of the UUV decreases. This means that smaller UUVs would be better equipped to overcome this hydrodynamic interaction.

A long slender body without control fins experiences a destabilizing effect when in steady translation. This is known as the munk moment (Newman, 2017). Also, the sway force increases as the heading angle increases, just like lift increases when the angle of attack increases on an airfoil. Fig. 14 shows how the sway and yaw coefficients vary based on the heading angle and speed of the UUV.

Fig. 14 shows that if the vehicle is at a non-zero heading angle, there is a resulting moment that will cause the vehicle to rotate in the direction in which it is angled. The surrogate model is able to accurately predict the munk moment of the UUV and the expected behavior of how it increases nearly linearly with heading angle (Fossen, 2011). The same relationship between heading angle and sway exists and the reduced order model accurately captures this phenomenon as well. Additionally, because the sway and yaw coefficients are non-dimensionalized using the velocity of the vehicle, these non-dimensional coefficients are expected to be relatively independent of the speed (Newman, 2017; Fossen, 2011). The surrogate model is also able to capture this effect.

The total drag on a submarine or UUV is a combination of its pressure (form) drag, caused by wake formation and boundary layer separation, and its viscous (skin) drag, caused by the fluid friction on the wetted surface of the vehicle. Vehicles have an optimal length to diameter ratio that reduces the drag on the vehicle (Burcher and Rydill, 1995). When vehicles are very short, they are more like bluff bodies and have a lot of pressure drag. As the vehicle becomes longer, the form drag decreases. However, when they become too long, the increase in viscous drag outweighs the loss in pressure drag. This means that a UUV has an optimal length to diameter ratio L/D_{UUV} for reducing drag. The optimal L/D_{UUV} is dependent on the shape and speed of the vehicle and is usually in the range of 8 to 12. Fig. 15 shows how the surge coefficient varies with L/D_{UUV}.

Fig. 15 shows that the minimum drag occurs with a UUV length to diameter ratio of about 10 to 12. This illustrates how the surrogate model is able to identify the trade-off between pressure drag and viscous drag for different UUV lengths. The optimal length to diameter

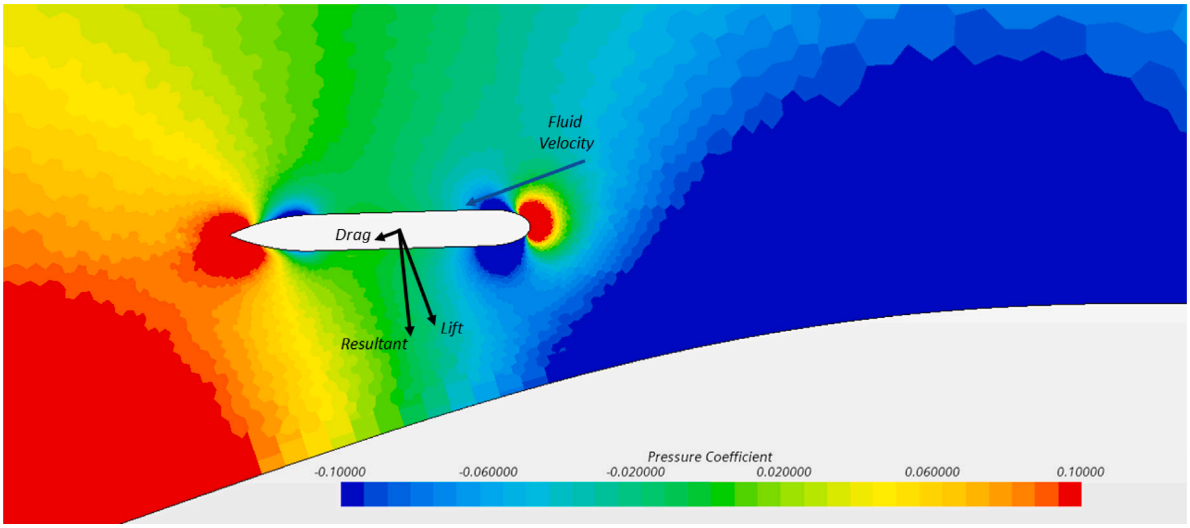

Fig. 13. Pressure field of the hydrodynamic interactions near the stern of the submarine with $R_{Long} = -0.3950$, $R_{Lat} = 0.06827$, $U = 4.410$ knots, $\phi = 1.617°$, $D_{Sub}/D_{UUV} = 23.41$, and $L/D_{UUV} = 8.329$. The steep pressure gradient and flow field result in the UUV experiencing a positive surge.

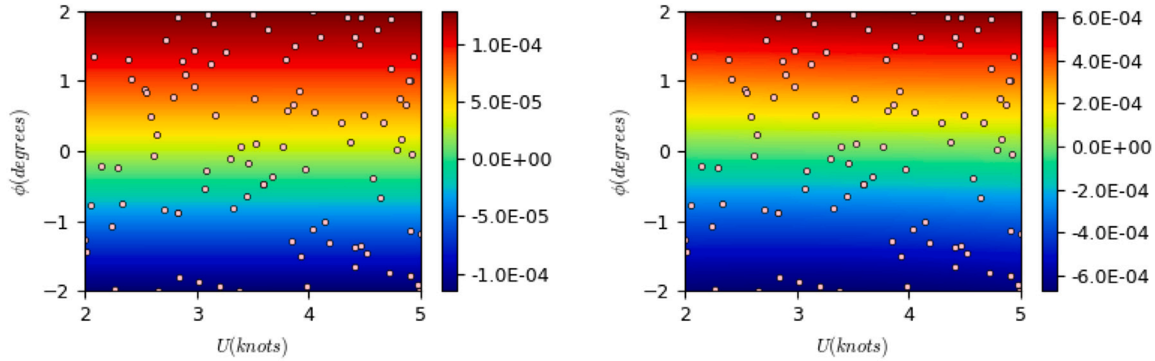

(a) Sway coefficient Y' of a UUV at various heading angles ϕ and speeds U with a fixed $R_{Long} = 0$, $R_{Lat} = 0.08$, $D_{Sub}/D_{UUV} = 20$, and $L/D_{UUV} = 8$. The reduced order model predicts a near-linear relationship been the sway and heading angle.

(b) Yaw coefficient N' of a UUV at various heading angles ϕ and speeds U with a fixed $R_{Long} = 0$, $R_{Lat} = 0.08$, $D_{Sub}/D_{UUV} = 20$, and $L/D_{UUV} = 8$. The reduced order model predicts a near-linear relationship been the yaw and heading angle.

Fig. 14. Maps of the sway and yaw coefficients Y' and N' at various heading angles ϕ and speeds U for a UUV with a fixed $R_{Long} = 0$, $R_{Lat} = 0.08$, $D_{Sub}/D_{UUV} = 20$, and $L/D_{UUV} = 8$.

ratio of submerged vessels is usually in this range, but varies based on shape and speed (Burcher and Rydill, 1995; Roddy, 1990). Additionally, the surrogate also found that the surge is relatively independent of small changes in heading angles. These results are consistent with real world results (Burcher and Rydill, 1995; Roddy, 1990). The gray region in Fig. 15(a) represents a constraint within the domain that is unexplored based on real-world UUV measurements which ignore the combination of UUV lengths and diameters that are infeasible.

Another benefit of the NMMF active learning GP regression process is that the process models the difference between the high fidelity (CFD) and low fidelity (potential flow) simulations. This means that the results of the model can be used to identify scenarios in which the low fidelity simulations fail to capture the accuracy of the high fidelity simulations. Fig. 16 compares the sway and yaw coefficients for the high fidelity surrogate model with the low fidelity model surrogate.

Fig. 16 shows that the low fidelity potential flow model is quite accurate at predicting the yaw coefficient, but has major limitations on predicting the sway coefficient due to the d'Alembert paradox (Newman, 2017; Fossen, 2011). Recall that the potential flow solver uses an empirical model to account for viscous effects in the surge direction. However, there are no viscous effects modeled in the sway direction using the potential flow solver so there results are inaccurate compared to the high fidelity CFD solver. Another example of this limitation is the inability of the low fidelity potential flow solver to determine the how the UUV sway is impacted by the UUV heading angle. Fig. 17 compares heading angles from the potential flow model with the high fidelity CFD model. This shows how potential flow is not able to accurately capture how the sway coefficient varies with changes to the heading angle. Because the potential flow solver neglects viscosity, it predicts an almost constant near zero value at any heading angle. This is inaccurate as seen by the high fidelity CFD solver. However, because the munk moment is a potential flow phenomenon and is the dominant source of UUV yaw, the potential flow solver is relatively accurate at determining the UUV yawing moment.

Because the d'Alembert paradox is a known limitation of potential solvers, many of them have built-in parametric models that augment the results. The d'Alembert paradox results in potential flow predicting zero drag around the UUV in steady state translation. In order to provide more accurate results, the FS-Flow potential flow solver uses the ITTC-57 parametric equations to estimate the drag of the UUV (Anon,

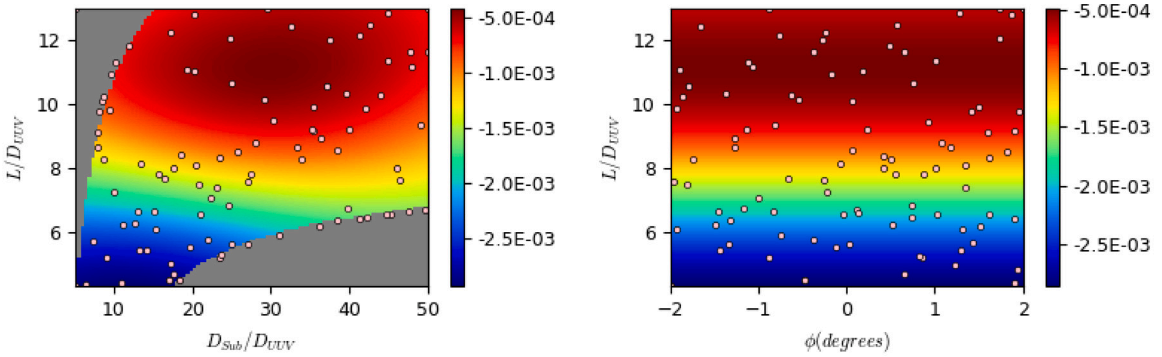

(a) Surge coefficient X' of a UUV with various L/D_{UUV} and D_{Sub}/D_{UUV} for a fixed $R_{Long} = 0$, $R_{Lat} = 0.08$, $U = 3.5$ knots, and $\phi = 0°$. UUVs with a small L/D_{UUV} experience more pressure drag so optimal $L/D_{UUV} \approx 10 - 12$.

(b) Surge coefficient X' of a UUV at various L/D_{UUV} and ϕ for a fixed $R_{Long} = 0$, $R_{Lat} = 0.08$, $U = 3.5$ knots, and $D_{Sub}/D_{UUV} = 20$. UUVs with a small L/D_{UUV} experience more pressure drag so optimal $L/D_{UUV} \approx 10 - 12$.

Fig. 15. Maps of the surge coefficient X' at various L/D_{UUV} for a UUV with a fixed $R_{Long} = 0$, $R_{Lat} = 0.08$, and $U = 3.5$ knots. This demonstrates the prediction of optimal L/D_{UUV}.

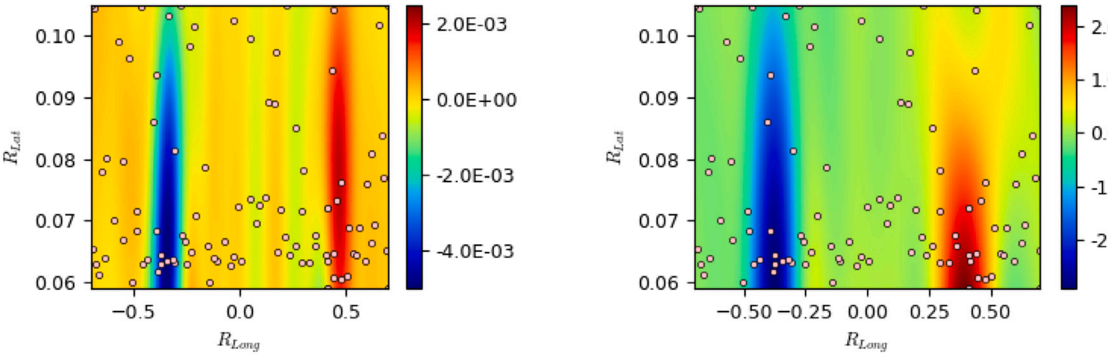

(a) High fidelity surrogate model prediction of the sway coefficient Y' of a UUV at various R_{Lat} and R_{Long} for a fixed $U = 3.5$ knots, $\phi = 0°$, $D_{Sub}/D_{UUV} = 20$ and $L/D_{UUV} = 8$.

(b) High fidelity surrogate model prediction of the yaw coefficient N' of a UUV at various R_{Lat} and R_{Long} for a fixed $U = 3.5$ knots, $\phi = 0°$, $D_{Sub}/D_{UUV} = 20$ and $L/D_{UUV} = 8$.

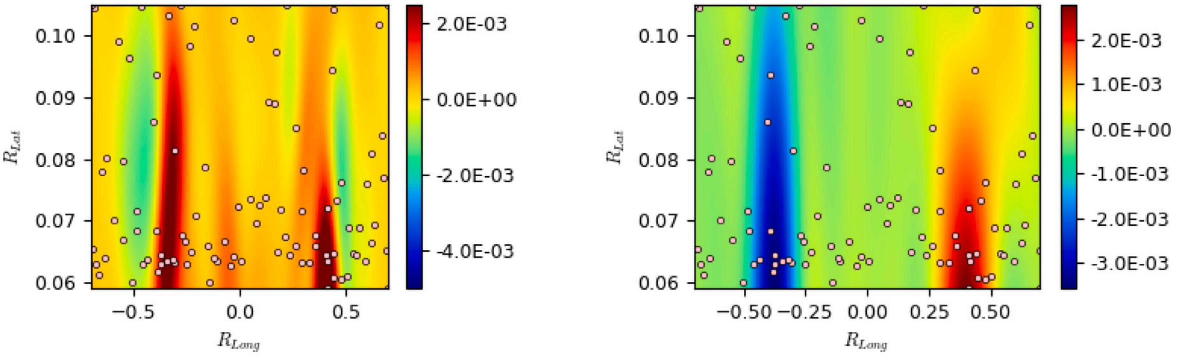

(c) Low fidelity surrogate model prediction of the sway coefficient Y' of a UUV at various R_{Lat} and R_{Long} for a fixed $U = 3.5$ knots, $\phi = 0°$, $D_{Sub}/D_{UUV} = 20$ and $L/D_{UUV} = 8$.

(d) Low fidelity surrogate model prediction of the yaw coefficient N' of a UUV at various R_{Lat} and R_{Long} for a fixed $U = 3.5$ knots, $\phi = 0°$, $D_{Sub}/D_{UUV} = 20$ and $L/D_{UUV} = 8$.

Fig. 16. Comparison of sway and yaw coefficients of the high and low fidelity surrogate models of a UUV at various R_{Lat} and R_{Long} for a fixed $U = 3.5$ knots, $\phi = 0°$, $D_{Sub}/D_{UUV} = 20$ and $/D_{UUV} = 8$. Low fidelity cannot accurately predict sway coefficient Y', but performs well for yaw coefficient N'.

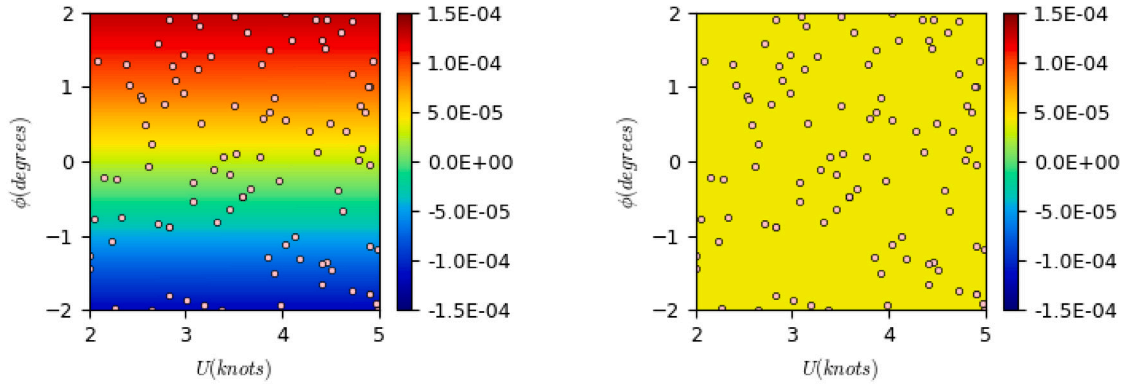

(a) High fidelity surrogate model prediction of the sway coefficient Y' of a UUV at various heading angles ϕ and speeds U with a fixed $R_{Long} = 0$, $R_{Lat} = 0.08$, $D_{Sub}/D_{UUV} = 20$, and $L/D_{UUV} = 8$. This accurately reflects expected the near-linear relationship between sway and heading angle.

(b) Low fidelity surrogate model prediction of the sway coefficient Y' of a UUV at various heading angles ϕ and speeds U with a fixed $R_{Long} = 0$, $R_{Lat} = 0.08$, $D_{Sub}/D_{UUV} = 20$, and $L/D_{UUV} = 8$. This predicts a constant near-zero value as expected by the d'Alembert paradox.

Fig. 17. Comparison of sway and yaw coefficients of the high and low fidelity surrogate models of a UUV at various heading angles ϕ and speeds U with a fixed $R_{Long} = 0$, $R_{Lat} = 0.08$, $D_{Sub}/D_{UUV} = 20$, and $L/D_{UUV} = 8$. Low fidelity cannot to accurately predict sway coefficient Y' due to the d'Alembert paradox.

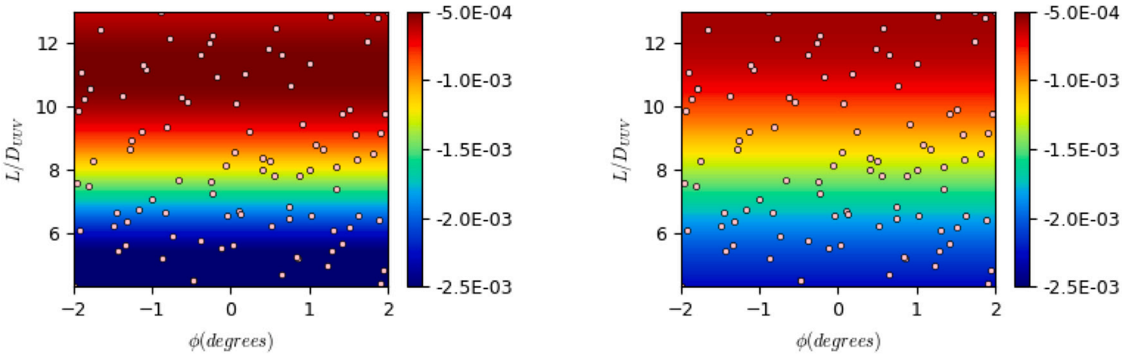

(a) High fidelity surrogate model prediction of the surge coefficient X' of a UUV at various L/D_{UUV} and heading angles ϕ with a fixed $R_{Long} = 0$, $R_{Lat} = 0.08$, $U = 3.5$ knots, and $D_{Sub}/D_{UUV} = 20$.

(b) Low fidelity surrogate model prediction of the surge coefficient X' of a UUV at various L/D_{UUV} and heading angles ϕ with a fixed $R_{Long} = 0$, $R_{Lat} = 0.08$, $U = 3.5$ knots, and $D_{Sub}/D_{UUV} = 20$.

Fig. 18. Comparison of surge coefficient X' of the high and low fidelity surrogate models of a UUV at various L/D_{UUV} and heading angles ϕ with a fixed $R_{Long} = 0$, $R_{Lat} = 0.08$, $U = 3.5$ knots, and $D_{Sub}/D_{UUV} = 20$. The ITTC-57 parametric equations of the low fidelity potential flow simulations are similar to the results of the high fidelity CFD simulations.

2018). Fig. 18 compares the surge coefficients of the high fidelity CFD surrogate model and the low fidelity potential flow surrogate model at various UUV length to diameter ratios.

Overall, the built-in ITTC-57 parametric equations of the low fidelity potential flow model are very similar to the model trained on CFD data. This allows the potential flow model to predict the surge coefficient much better than the sway coefficient.

In order to test the accuracy of the model, a total of 500 Latin Hypercube samples are used as test data for the GP regression model. Latin Hypercube sampling is a common method used to divide each dimension of a multi-dimensional input domain into equally spaced bins in order to ensure a good distribution of sampling locations within the domain (Stein, 1987). The mean absolute error (MAE) between the predicted and actual results of the test data is determined for each of the three outputs. Because these values are hard to conceptualize, MAE can be thought of in terms of the control system of the UUV and how these errors translate into UUV control values. The MAE of the sway and yaw coefficients can be represented as an equivalent rudder angle difference $\Delta\delta_{eq,Y}$ or $\Delta\delta_{eq,N}$. This is how much the rudder angle would need to change to produce the force or moment equivalent to the MAE. Likewise, the surge coefficient MAE can be thought of as a percentage of the propulsive force of the UUV ($\%X_{prop}$). The hydrodynamic coefficients in use to determine these error equivalents in Table 2 are taken from the Remus 100 (Winey, 2020).

Table 2
Mean absolute error and error equivalents of the various model outputs.

Output	Mean absolute error	Error equivalents
X'	7.492E–04	10.26% X_{prop}
Y'	7.220E–04	$\Delta\delta_{eq,Y} = 1.78$ degrees
N'	7.629E–04	$\Delta\delta_{eq,N} = 3.95$ degrees

Overall, the reduced order model is able to predict the complex surge, sway, and yaw hydrodynamic interactions that are determined using the CFD simulations and validated against tow tank experiments. This reduced order model can be used to determine the hydrodynamic interactions in real time, which is several orders of magnitude faster than performing a CFD simulation, which usually takes several hours to complete.

7. Conclusions

We have formulated a new method for active sampling that is non-myopic and also utilizes models of multiple fidelity. The new approach allows for efficiently computing reduced-order models with unprecedented accuracy due to its non-myopic active search properties. It is ideal for situations where plentiful and accurate training data is not easy to obtain, e.g. because of high computational cost. We have first demonstrated the advantages of the new approach in two representative prototype systems, as well as a more realistic setup involving the hydrodynamic interactions between a UUV and a submarine.

The non-myopic multi-fidelity active learning GP regression surrogate model is able to accurately predict the complex hydrodynamic interactions between a submarine and UUV. Specifically, the obtained model is able to mimic the high accuracy of the CFD while being able to predict these hydrodynamic interactions in real-time. Real-time modeling of these hydrodynamic interactions is essential to simulate the motion required to launch and recover UUVs from submarines. To this end, this surrogate model may be integrated into UUV control and autonomy systems and motion simulators to predict these hydrodynamic interactions and further enable UUV launch and recovery from submarines. We leave this direction as future work.

Other future directions may include increasing the dimensionality of the input space by considering more parameters, i.e. more complex and realistic setups. Such a step would require more effective surrogate models such as those based on neural networks or operators (Pickering et al., 2022). This could include introducing movable control surfaces on the UUV, modeling transient UUV behavior, accounting for six degrees of freedom motion by allowing the two vehicle axes to be non-planar, or simulating the hydrodynamic interactions near a submarine appendage like the sail or a dry deck shelter. In addition, the application of this non-myopic multi-fidelity sampling algorithm is currently formulated for only two levels of fidelity. An extension to more levels of future work.

CRediT authorship contribution statement

Brady Hammond: Conceptualization, Software, Methodology, Investigation, Funding acquisition, Writing – original draft. **Themistoklis P. Sapsis:** Conceptualization, Methodology, Supervision, Investigation, Funding acquisition, Software, Writing – original draft.

Declaration of competing interest

The authors declare that they have no known competing financial interests or personal relationships that could have appeared to influence the work reported in this paper.

Data availability

No data was used for the research described in the article.

Acknowledgments

BH has been supported as a Ph.D. student by the MIT 2N Navy Program. TPS has been supported by the ONR, United States Grants ONR - N00014-21-1-2357 and N00014-20-1-2366. Discussions with the following individuals and teams are also greatly appreciated.

- Chris Harding, Geoffrey McNally, and team - Warfare Integrated Systems Branch, Naval Undersea Warfare Center
- Daniel Milligan and team - Undersea Vehicles Lead, General Dynamics Electric Boat
- Joel Parry and team - Maritime Warfare and ISR, Business Area Lead, Draper
- Sasha Tsarev - Maritime Systems Hydromechanics Branch, Naval Surface Warfare Center
- David A. Drazen - Chief Technology Officer, Naval Surface Warfare Center
- CDR Kyle Weorner - Program Manager, Tactical Technology Office, Defense Advanced Research Projects Agency

References

Anon, 2018. FS-Flow User manual. URL: www.dnvgl.com.

Blanchard, A., Sapsis, T., 2021. Output-weighted optimal sampling for Bayesian experimental design and uncertainty quantification. SIAM/ASA J. Uncertain. Quantif. 9, 564–592.

Burcher, Roy, Rydill, Louis J., 1995. Concepts in Submarine Design. Cambridge University Press, ISBN: 978-1-139-92723-9.

Chaloner, K., Verdinelli, I., 1995. Bayesian experimental design: A review. Statist. Sci. 10, 273–304.

Constans, Eric, 2013. How to simulate a trebuchet Part 2: Equations of motion. URL: http://www.benchtophybrid.com/TB_index.html.

Damianou, Andreas, Lawrence, Neil D., 2013. Deep Gaussian processes. In: Carvalho, Carlos M., Ravikumar, Pradeep (Eds.), Proceedings of the Sixteenth International Conference on Artificial Intelligence and Statistics. In: Proceedings of Machine Learning Research, vol. 31, PMLR, Scottsdale, Arizona, USA, pp. 207–215, URL: https://proceedings.mlr.press/v31/damianou13a.html.

Explorer AUV, 2020. International submarine engineering. URL: https://ise.bc.ca/product/explorer/ (visited on 09/09/2020).

Fedor, Robert, 2009. Simulation of a Launch and Recovery of an UUV to an Submarine (Thesis). Royal Institute of Technology.

Fossen, Thor I, 2011. Handbook of Marine Craft Hydrodynamics and Motion Control. John Wiley & Sons, Ltd, ISBN: 978-1-119-99149-6.

Gertler, Morton, Hagen, Grant R., 1967. Standard Equations of Motion for Submarine Simulation. Naval Ship Recearch and Development Center.

Gonzalez, Javier, Osborne, Michael, Lawrence, Neil D., 2015. GLASSES: Relieving the Myopia of Bayesian optimisation. In: Proceedings of the 19th International Conference on Artificial Intelligence and Statistics (AISTATS).

Gramacy, R.B., Lee, H.K., 2009. Adaptive design and analysis of supercomputer experiments. Techno- metrics 51, 130–145.

Grassi, Francesco, Manganini, Giorgio, Garraffa, Michele, Mainini, Laura, 2020. Resource aware multifidelity active learning for efficient optimization. arXiv:2007.04674 [cs.LG].

Groves, Nancy C., Huang, Thomas T., Chang, Ming S., 1989. Geometric characteristics of DARPA SUBOFF models.

Harper, William V., Gupta, Sumant K., 1983. Sensitivity/uncertainty analysis of a borehole scenario comparing latin hypercube sampling and deterministic sensitivity approaches. In: Office of Nuclear Waste Isolation.

Jiang, Shali, Malkomes, Gustavo, Converse, Geoff, Shofner, Alyssa, Moseley, Benjamin, Garnett, Roman, 2017. Efficient nonmyopic active search. In: Proceedings of the 34 th International Conference on Machine Learning. p. 10.

Kennedy, M., 2000. Predicting the output from a complex computer code when fast approximations are available. Biometrika 87 (1), 1–13. http://dx.doi.org/10.1093/biomet/87.1.1, URL: https://academic.oup.com/biomet/article-lookup/doi/10.1093/biomet/87.1.1 (visited on 01/13/2022), ISSN: 0006-3444, 1464-3510.

Leong, Zhi Quan, 2014. Effects of Hydrodynamic Interaction on an AUV Operating Close to a Moving Submarine. Australian Maritime College, University of Tasmania.

Leong, Saad, Ranmuthugala, Duffy, 2013. Investigation into the Hydrodynamic Interaction Effects on an AUV Operating Close to a Submarine. Australian Maritime College, University of Tasmania.

Menter, F.R., 1994. Two-equation eddy-viscosity turbulence models for engineering applications. AIAA J. 32 (8), 1598–1605. http://dx.doi.org/10.2514/3.12149, URL: https://arc.aiaa.org/doi/10.2514/3.12149 (visited on 08/18/2020), ISSN: 0001-1452, 1533-385X.

Moonesun, Mohammad, Korol, Yuri, Dalayeli, Hosein, 2015. CFD analysis on the bare hull form of submarines for minimizing the resistance. Int. J. Marit. Technol. 16.

Morere, Philippe, Marchant, Roman, Ramos, Fabio, 2016. Bayesian optimisation for solving continuous state-action-observation POMDPs. In: 30th Conference on Neural Information Processing Systems. p. 5.

Newman, J.N., 2017. Marine Hydrodynamics, 40th Anniversary ed. MIT Press, ISBN: 978-0-262-53482-6.

Osborne, Michael A., Garnett, Roman, Roberts, Stephen J., 2008. Gaussian processes for global optimization.

Perdikaris, P., Raissi, M., Damianou, A., Lawrence, N.D., Karniadakis, G.E., 2017. Nonlinear information fusion algorithms for data-efficient multi-fidelity modelling. Proc. R. Soc. A 473 (2198), 20160751. http://dx.doi.org/10.1098/rspa.2016.0751, URL: https://royalsocietypublishing.org/doi/10.1098/rspa.2016.0751 (visited on 10/04/2021), ISSN: 1364-5021, 1471-2946.

Perdikaris, P., Venturi, D., Royset, J.O., Karniadakis, G.E., 2015. Multi-fidelity modelling via recursive co-kriging and Gaussian-Markov random fields. Proc. Math. Phys. Eng. Sci. / R. Soc. (ISSN: 1364-5021) 471 (2179), 20150018. http://dx.doi.org/10.1098/rspa.2015.0018, URL: http://rspa.royalsocietypublishing.org/content/471/2179/20150018.

Pickering, E., Guth, S., Karniadakis, G., Sapsis, T., 2022. Discovering and forecasting extreme events via active learning in neural operators. Nature Computational Science 19, URL: https://www.nature.com/articles/s43588-022-00376-0.

2014. Practical guidelines for ship CFD applications. In: International Towing Tank Conference - 7.5–03–02–03.

Rasmussen, Carl Edward, Williams, Christopher K.I., 2006. Gaussian Processes for Machine Learning. In: Adaptive Computation and Machine Learning, MIT Press, ISBN: 978-0-262-18253-9, OCLC: ocm61285753.

Roddy, Robert F., 1990. Investigation of the Stability and Control Characteristics of Several Configurations of the DARPA SUBOFF Model (DTRC Model 5470) from Captive-Model Experiments. David Taylor Research Center.

Rutan, Shawn, Wieczorek, Becky, 2005. Modern siege weapons: Mechanics of the Trebuchet.

Sacks, J., Welch, W.J., Mitchell, T.J., 1989. Design and analysis of computer experiments. Statist. Sci. 4, 409–423.

Siano, Donald B., 2013. Trebuchet mechanics.

Stein, Michael, 1987. Large sample properties of simulations using latin hypercube sampling. Technometrics 29 (2), 143–151. http://dx.doi.org/10.1080/00401706.1987.10488205.

Surjanovic, Sonja, Bingham, Derek, 2013. Virtual Library of Simulation Experiments: Test Functions and Datasets. URL: https://www.sfu.ca/∼ssurjano/index.html.

Takeno, Shion, Fukuoka, Hitoshi, Tsukada, Yuhki, Koyama, Toshiyuki, Shiga, Motoki, Takeuchi, Ichiro, Karasuyama, Masayuki, 2020. Multi-fidelity Bayesian optimization with max-value entropy search and its parallelization. In: Proceedings of the 37th International Conference on Machine Learning. ICML '20, JMLR.org.

Wilson, Andrew Gordon, Adams, Ryan Prescott, 2013. Gaussian process kernels for pattern discovery and extrapolation. In: Proceedings of the 30 th International Conference on Machine Learning. p. 9.

Winey, Nastasia E., 2020. Modifiable Stability and Maneuverability of High Speed Unmanned Underwater Vehicles (UUVs) Through Bioinspired Control Fins. Massachusetts Institute of Technology and Woods Hole Oceanographic Institution, Woods Hole, MA, http://dx.doi.org/10.1575/1912/26053, URL: https://hdl.handle.net/1912/26053 (visited on 03/10/2021).

Xiong, Shifeng, Qian, Peter Z.G., Wu, C.F. Jeff, 2013. Sequential design and analysis of high-accuracy and low-accuracy computer codes. Technometrics 55 (1), 37–46. http://dx.doi.org/10.1080/00401706.2012.723572, URL: https://www.tandfonline.com/doi/full/10.1080/00401706.2012.723572 (visited on 01/10/2022), ISSN: 0040-1706, 1537-2723.